

# JGR Planets

## RESEARCH ARTICLE

10.1029/2020JE006651

### Key Points:

- We present density and P-wave velocity measurements of Fe-Si-C liquid metal up to 5.8 GPa and 2000 K
- Interior structure models for Mercury are calculated and constrained by geodetic observations to examine consequences of various core compositions
- Implications of the results for Mercury's bulk composition, formation, and dynamo generation are discussed

### Supporting Information:

- Supporting information S1

### Correspondence to:

J. S. Knibbe,  
[j.s.knibbe@vu.nl](mailto:j.s.knibbe@vu.nl)













### Citation:

Knibbe, J. S., Rivoldini, A., Luginbuhl, S. M., Namur, O., Charlier, B., Mezouar, M., et al. (2021). Mercury's interior structure constrained by density and P-wave velocity measurements of liquid Fe-Si-C alloys. *Journal of Geophysical Research: Planets*, 126, e2020JE006651. <https://doi.org/10.1029/2020JE006651>

Received 9 AUG 2020

Accepted 23 NOV 2020

## Mercury's Interior Structure Constrained by Density and P-Wave Velocity Measurements of Liquid Fe-Si-C Alloys

J. S. Knibbe<sup>1,2,3,4</sup> , A. Rivoldini<sup>3</sup> , S. M. Luginbuhl<sup>2</sup> , O. Namur<sup>1</sup> , B. Charlier<sup>5</sup> , M. Mezouar<sup>6</sup> , D. Sifre<sup>6</sup> , J. Berndt<sup>7</sup> , Y. Kono<sup>8</sup> , D. R. Neuville<sup>9</sup> , W. van Westrenen<sup>2</sup> , and T. Van Hoolst<sup>3,4</sup> 

<sup>1</sup>Department of Earth and Environmental Sciences, KU Leuven, Leuven, Belgium, <sup>2</sup>Department of Earth Sciences, Faculty of Science, VU University Amsterdam, Amsterdam, The Netherlands, <sup>3</sup>Royal Observatory of Belgium, Brussels, Belgium, <sup>4</sup>Institute of Astronomy, KU Leuven, Leuven, Belgium, <sup>5</sup>Department of Geology, University of Liège, Sart Tilman, Belgium, <sup>6</sup>European Synchrotron Radiation Facility (ESRF), Grenoble, France, <sup>7</sup>Institute for Mineralogy, Westfälische Wilhelms-Universität Münster, Münster, Germany, <sup>8</sup>Geodynamics Research Center, Ehime University, Ehime, Japan, <sup>9</sup>Université de Paris, Institut de Physique du Globe de Paris, CNRS, Paris, France

**Abstract** Experimental measurements of density by X-ray absorption and of P-wave velocity by ultrasonic techniques of liquid Fe-( $<17$  wt%) Si-( $<4.5$  wt%) C alloys at pressures up to 5.8 GPa are presented. These data are used to construct an Fe-Si-C liquid mixing model and to characterize interior structure models of Mercury with liquid outer core composed of Fe-Si-C. The interior structure models are constrained by geodetic measurements of the planet, such as the obliquity and libration of Mercury. The results indicate that S and/or C with concentrations at the wt% level are likely required in Mercury's core to ensure the existence of an inner core with a radius (below  $\sim 1,200$  km) that is consistent with reported dynamo simulations for Mercury's magnetic field. Interior structure models with more than 14 wt% Si in the core, estimated for Mercury by assuming an EH chondrite-like bulk composition, are only feasible if the obliquity of Mercury is near the upper limit of observational uncertainties (2.12 arcmin) and the mantle is dense ( $3.43\text{--}3.68\text{ g}\cdot\text{cm}^{-3}$ ). Interior structure models with the central obliquity value (2.04 arcmin) and less than 7.5 wt% Si in the core, consistent with estimates of Mercury's core composition from an assumed CB chondrite-like bulk composition, are compatible with  $3.15\text{--}3.35\text{ g}\cdot\text{cm}^{-3}$  mantle densities and an inner core radius below 1,200 km. Interior structure models with the obliquity of Mercury near the lower observational uncertainty limit (1.96 arcmin) have a low-density mantle ( $2.88\text{--}3.03\text{ g}\cdot\text{cm}^{-3}$ ), less than 4 wt% Si in the core, and an inner core radius larger than 1,600 km.

**Plain Language Summary** Mercury's large core is critical for understanding Mercury's composition and magnetic field, which is driven by core convection. Inferring Mercury's core composition from gravitational and rotational parameters requires a relation between density and composition of plausible core materials at high pressures and temperatures. This study presents experimental data that constrain the relation between density and composition of liquid Fe-Si-C metal alloys at pressures up to 5.8 GPa and temperatures of about 2000 K. The experimental results are integrated in interior structure models of Mercury to examine the range of possible core compositions. We conclude that only limited concentrations of silicon, carbon, and sulfur can be present in Mercury's core. High Si core concentrations, consistent with an EH chondrite-like bulk composition for Mercury, would require a high density of Mercury's mantle and a large inner core. The lower Si core concentrations expected from a CB chondrite-like bulk composition for Mercury place less stringent requirements on the planet. Carbon and/or sulfur in the liquid outer core can induce compositional buoyancy that is relevant for the generation of magnetic field in Mercury's core.

## 1. Introduction

The unusual bulk composition of planet Mercury, particularly its anonymously large iron (Fe)-fraction of 60–80 wt% that is inferred from the planet's high density (Rabe, 1950; Urey, 1951), has led to a strong interest in Mercury's formation history. It is generally assumed that the proto-Mercury formed by accretion of solar nebula condensates, out of which a metallic core and a silicate mantle segregated under influence of gravity (e.g., Urey, 1951). Planetary formation scenarios that attempt to explain the large Fe-fraction of

Mercury include: (1) the accretion of dominantly Fe-rich solar nebula condensates (Hubbard, 2014; Weidenschilling, 1978; Wurm et al., 2013), (2) the stripping of silicate mantle material from a significantly larger proto-Mercury by one or multiple giant impacts (Asphaug & Reufer, 2014; Benz et al., 1988; Chau et al., 2018), and (3) the evaporation of (particularly alkali-rich) silicates from a significantly larger proto-Mercury (Cameron, 1985; Fegley & Cameron, 1987). NASA's Mercury Surface, Space Environment, Geochemistry, and Ranging (MESSENGER) space mission revealed that Mercury's surface is rich in sulfur (S), sodium (Na), and potassium (K), and poor in Fe (Nittler et al., 2011; Peplowski et al., 2011, 2014). The high surface abundances of volatile elements S, Na, and K are difficult to reconcile with the silicate-evaporation scenario (Charlier & Namur, 2019; Nittler et al., 2011; Peplowski et al., 2011, 2014). It remains difficult to validate or falsify formation scenarios (1) and (2) based on present-day geochemical data of the Mercury's surface (Charlier & Namur, 2019; Ebel & Stewart, 2018; Nittler et al., 2018). To this end, an improved understanding of the consequences of these formation scenarios as well as improved constraints on Mercury's bulk composition are needed. A profound understanding of the composition of Mercury's core is important to constrain Mercury's bulk composition, formation scenarios, and possible building blocks of the planet (for example, the EH and CB chondrites).

The low surface abundance of Fe and high surface abundance of S suggest a low oxygen fugacity for Mercury of between 3.2 and 7.3 logarithmic units below the Fe-FeO buffer (McCubbin et al., 2017; Namur et al., 2016; Zolotov et al., 2013). Metal-silicate fractionation experiments show that the concentration of S in Fe-rich metal is limited to ~2 wt% at such strongly reducing conditions (e.g., Boujibar et al., 2014; Chabot et al., 2014; Namur et al., 2016). In contrast, silicon (Si) behaves increasingly siderophile at reducing conditions (e.g., Berthet et al., 2009; Cartier et al., 2014; Chabot et al., 2014; Kilburn & Wood, 1997; Namur et al., 2016; Steenstra et al., 2020). Carbon (C) has also been measured at Mercury's surface and may be present in Mercury's core (Peplowski et al., 2015; Steenstra & van Westrenen, 2020; Vander Kaaden et al., 2020). The solubility of C in Fe-rich metal decreases with Si-concentrations from ~6 wt% in liquid pure Fe metal (Dasgupta & Walker, 2008; determined from experiments at 2273–2683 K and 2 GPa) to ~1 wt% in Fe-17 wt% Si (Li et al., 2016; Steenstra et al., 2020; Vander Kaaden et al., 2020). Temperature and pressure also influence the solubility of C in Fe-rich metal, but those effects are thought to be subordinate to the influence of Si at the conditions relevant for Mercury (Steenstra et al., 2020; Vander Kaaden et al., 2020; and references therein). In light of the low oxygen fugacity inferred for Mercury, it is therefore likely that Si is the dominant light constituent of Mercury's core, potentially combined with smaller amounts of C and S (e.g., Chabot et al., 2014; Steenstra & van Westrenen, 2020; Vander Kaaden et al., 2020).

Mercury's magnetic field is weaker than expected for a Mercury-sized planet with an active core dynamo (Christensen, 2006; Ness, 1979). It has a broad-scale dipole-and-quadrupole dominated geometry (Anderson et al., 2012), although a dynamo in an object that rotates as slowly as Mercury does (59-day rotational period) is expected to be dominated by small-scale rapidly varying structures (Christensen, 2006). The majority of recent dynamo simulations explain the low strength and broad-scale geometry of Mercury's magnetic field by a configuration with sufficiently vigorous core convection for dynamo action deep in the liquid core and a stably stratified upper part of the liquid core that attenuates rapidly varying field components (e.g., Cao et al., 2014; Christensen, 2006; Christensen & Wicht, 2008; Manglik et al., 2010; Takahashi et al., 2019; Tian et al., 2015; Wardinski et al., 2020). Dynamo simulations that obtain a dipole and/or quadrupole dominated broad-scale magnetic field with field intensity that is consistent with Mercury have been reported only with inner cores smaller than 1,200 km in radius (Cao et al., 2014; Christensen, 2006; Christensen & Wicht, 2008; Manglik et al., 2010; Takahashi et al., 2019; Tian et al., 2015). Those simulations that are additionally consistent with the dipole/quadrupole ratio of Mercury's magnetic field during short (cases 3 and 4 of Christensen & Wicht, 2008) or with long (Takahashi et al., 2019) simulated time periods have an inner core of ~1,000 or ~400 km in radius, respectively. Nonaxisymmetric features in Mercury's magnetic field at high northern latitudes might be indicative of an inner core radius between 500 and 660 km (Wardinski et al., 2020). The distribution and nature (thermal and/or compositional) of buoyancy in the liquid core play a prominent role in the core convection and dynamo action (Manglik et al., 2010; Takahashi et al., 2019) and are related to the light elements that are present in Mercury's core (e.g., Christensen & Wicht, 2008; Dumberry & Rivoldini, 2015; Knibbe & van Westrenen, 2018; Manglik et al., 2010). The partitioning of S and C (Fei et al., 1997; Fei & Brosh, 2014) into the liquid metal upon the solidification of an inner core may give rise

to compositional buoyancy in the liquid core (e.g., Manglik et al., 2010), whereas Si does not significantly fractionate upon core solidification (e.g., Kuwayama & Hirose, 2004).

Geophysical constraints on the interior mass distribution of Mercury are derived from geodetic measurements under the assumption that Mercury is in, or very near to, a stable rotational state that is referred to as a “Cassini state 1” (e.g., Margot et al., 2012). The compositional range of Mercury’s core for which the mass distribution of the planet is in agreement with geodetic measurements can be examined by core-composition-dependent planetary interior structure modeling (e.g., Dumberry & Rivoldini, 2015; Genova et al., 2019; Hauck et al., 2013; Knibbe & van Westrenen, 2015; Rivoldini & Van Hoolst, 2013). Such interior structure modeling requires a composition-dependent parametrization of the thermodynamic properties of the considered metallic core alloys. An important ingredient of the core model is the equation of state (EOS) of liquid Fe. Thermodynamic properties of liquid Fe at planetary core conditions are difficult to determine experimentally. Therefore, several published EOSs of liquid Fe are deduced from EOSs of solid Fe phases and the Fe liquidus by thermodynamic modeling (e.g., Dorogokupets et al., 2017; Komabayashi, 2014) or by density functional theory (e.g., Wagle & Steinle-Neumann, 2019).

The density and P-wave velocity ( $V_P$ ) of certain liquid metallic mixtures are experimentally measured at high pressure. Density measurements at high pressure on the liquid Fe-Si system and on the related liquid Fe-Si-( $\leq 10$  wt%)Ni system were performed by Sanloup et al. (2004), Tateyama et al. (2011), Yu and Secco (2008), Terasaki et al. (2019), and Morard et al. (2013). These density measurements are, however, in poor agreement. For example, density measurements of liquid Fe-17 wt% Si metal at 4 GPa vary between  $6.0 \text{ g}\cdot\text{cm}^{-3}$  at 1773 K (Yu & Secco, 2008) and  $\sim 6.8 \text{ g}\cdot\text{cm}^{-3}$  at 1923 K (Tateyama et al., 2011). Experimental measurements of the  $V_P$  of Fe-Si-5 wt% Ni liquids at ambient pressure show an increase of  $V_P$  with increasing Si-concentration and a decrease of  $V_P$  with temperature (Williams et al., 2015). These trends are confirmed by experimental  $V_P$  measurements on Fe-Si-10 wt% Ni liquids at pressures up to 12 GPa (Terasaki et al., 2019). High-pressure density measurements at pressures below 10 GPa and temperatures below 2000 K on liquid  $\text{Fe}_3\text{C}$  (Terasaki et al., 2010) and Fe-3.5 wt% C (Shimoyama et al., 2016) indicate that C lowers the density of Fe-rich liquid by  $\sim 0.75\%$  per wt% C. Measurements of  $V_P$  on liquid Fe-C alloys show a decrease of  $V_P$  with increasing concentration of C at low pressures ( $< 3.2$  GPa) (Shimoyama et al., 2016), and an increase of  $V_P$  with increasing concentration of C at high pressures (up to 71 GPa; Nakajima et al., 2015). Experimental measurements of density and  $V_P$  of ternary Fe-Si-C liquids at high pressures, relevant for the core of Mercury, are completely absent at present.

This study presents new measurements of density (Section 2.1) and  $V_P$  (Section 2.2) of binary Fe-Si and ternary Fe-Si-C liquids at pressures up to 6 GPa. An ideal ternary Fe-Si-C mixing model (FESIC) is calibrated to our experimental measurements and other literature data (Section 2.3). The FESIC model is implemented in interior structure models of Mercury that satisfy the constraints set by geodetic measurements (Section 2.4). Interior structure models are also constructed with small amounts of S incorporated in the core liquid. Results of the density and  $V_P$  measurements and the accompanying FESIC mixing model are presented, discussed, and compared to literature in Section 3. The interior models of Mercury are presented and discussed in relation to other constraints on Mercury in Section 4. The implications for Mercury’s building blocks and for magnetic field generation in Mercury are discussed in Sections 5.1 and 5.2, respectively.

## 2. Materials and Methods

### 2.1. Density Measurements of Liquid Fe-Si-C at High Pressure by X-Ray Absorption

Density measurements of Fe-Si-C liquid metals are performed by X-ray absorption techniques with a Paris-Edinburgh (PE) press at beamline ID-27 of the European Synchrotron Radiation Facility (ESRF) in Grenoble, France. Pure Fe, and pure Si metallic powders (Alfa Aesar) are mixed to form Fe-Si mixtures with 4.25 wt% Si (used in experiments Exp11 and Exp13), 8.5 wt% Si (used in experiments Exp1, Exp2, and Exp4), 14.5 wt% Si (used in experiments Exp8, Exp9, and Exp12), and 17 wt% Si (used in experiments Exp5, Exp6, and Exp7). Sample powder is loaded into a cylindrical diamond (C) sample container, which saturates the sample in C by chemical diffusion when the experiment is at high temperatures (Sanloup et al., 2011). The sample container is surrounded by boron-nitride (BN) lids and a BN cylinder. Pressure-temperature

calibrant powder is mixed from platinum (Pt) and magnesia (MgO) in 1:1 weight proportion and loaded in a hand-drilled hole in the BN cylinder. These parts are integrated in a standard 7 mm-diameter PE assembly of this beamline (van Kan-Parker et al., 2010). Angle dispersive X-ray (33.2 keV) spectra are acquired in situ to determine the (solid or liquid) state of the sample and to determine the density of the Pt and BN materials in contact with the outside of the diamond sample container. The latter X-ray spectra are used to estimate the experimental pressure and temperature conditions through isochore-crossings of corresponding Pt and BN EOSs (Table A3 of the supporting information).

The density of the sample at experimental conditions ( $\rho_{S,PT}$ ) is calculated by

$$\rho_{S,PT} = \rho_{S,0} \frac{\rho_{S,PT} \mu_S}{\rho_{S,0} \mu_S},$$

where  $\rho_{S,PT} \mu_S$ , with  $\mu_S$  the mass absorption coefficient of the sample, is determined by fitting the Beer-Lambert law for X-ray absorption to the X-ray absorption profiles that are collected in situ,  $\rho_{S,0} \mu_S$  is determined by fitting the Beer-Lambert law to the X-ray absorption profiles that are collected at ambient conditions after quenching and decompression, and  $\rho_{S,0}$ , which denotes the sample density at ambient conditions, is measured by hydrostatic weighing at the Institut de Physique du Globe in Paris, France. A full description of the density experiments, data processing, and fitting procedures is available in Text A of supporting information. The chemical compositions of the samples that are successfully recovered from the hydrostatic weighing are analyzed by electron microprobe at the Westfälische-Wilhelms University Münster, Germany. The microprobe analysis is described in Text B of supporting information.

## 2.2. Ultrasonic P-Wave Velocity ( $V_p$ ) Measurements of Liquid Fe-Si-C at High Pressure

Ultrasonic  $V_p$  measurements of Fe-Si liquid metals are performed with a PE press at beamline 16-BM-B of the Advanced Photon Source (APS) synchrotron facility, in Argonne, Illinois. At the time of measurements, this beamline was operated by HP-CAT of the Geophysical Laboratory of the Carnegie Institution for Science. Sample powder of either Fe-17 wt% Si (Goodfellow Inc., 99.9 purity) or Fe-10 wt% Si, obtained by mixing with pure Fe (Alfa Aesar, 99.9 purity), is loaded in a cylindrical BN sample container. The sample and BN container are enclosed by polished alumina buffer rods ( $\text{Al}_2\text{O}_3$ ). These are integrated in a standard 7 mm-diameter PE assembly for ultrasonic measurements of this beamline (Kono et al., 2012; Figure C1 of supporting information). Energy dispersive X-ray spectra of the sample are acquired in situ at  $15.008^\circ$  angle to monitor the state of the sample (solid or liquid; Figure C2 in supporting information). Additional in situ X-ray spectra are acquired of the  $\text{Al}_2\text{O}_3$  and BN assembly parts that surround the sample, which are used to determine the experimental pressure and temperature conditions from isochore-crossings of corresponding  $\text{Al}_2\text{O}_3$  and BN EOSs (Table C1 of supporting information). Ultrasonic signals of 20, 25, and 30 MHz are generated and received by a lithium niobite ( $\text{LiBNO}_3$ ) transducer that is located at the top of the setup. Vertical wave reflections at the top (R1) and at the bottom (R2) of the sample are recorded and used to determine the vertical two-way travel time ( $\theta = t(R2) - t(R1)$ ) of the ultrasonic wave through the sample. The sample length ( $D$ ) is determined from radiographic images that are collected in situ. The P-wave velocity follows from  $V_p = \theta / (2D)$ . For both sample powders, we collected multiple measurements in a series of heating cycles at a range of pressures. The experiment is ended when the sample is thinned too much by compression for obtaining useful ultrasonic data.

A full description of the  $V_p$  experiments and the data analysis is available in text C of supporting information. Both the Fe-17 wt% Si (FeSi17) sample and the Fe-10 wt% Si (FeSi10) sample are analyzed by electron microprobe at the Westfälische-Wilhelms University Münster, Germany (Text B of supporting information).

## 2.3. Development of a Mixing Model for Ternary Liquid Fe-Si-C

Liquid Fe-Si-C is modeled by an ideal ternary mixing model (FESIC) that uses pure Fe, FeSi (Fe-33.5 wt% Si) and  $\text{Fe}_3\text{C}$  (Fe-6.7 wt% C) as endmembers. The EOS for l-Fe of Komabayashi (2014) is adopted for the Fe



endmember. EOS parameters for the FeSi and Fe<sub>3</sub>C endmembers are obtained by fitting the solution model to the experimental data. The limited ranges of pressure and sample composition that are spanned by the density and  $V_p$  measurements of this study are insufficient to constrain all relevant EOS parameters of the FeSi and Fe<sub>3</sub>C endmembers. For this reason, additional experimental ambient-pressure density (Jimbo & Cramb, 1993; Kawai 1974) and  $V_p$  (Pronin et al., 1964; Williams et al., 2015) measurements as well as high-pressure (1.2–3.4 GPa) density and  $V_p$  measurements of binary Fe-3.5 wt% C liquids (Shimoyama et al., 2016) from literature are incorporated in the fitting procedure. The FESIC mixing model is compared to nonideal Fe-Si and Fe-S mixing models of Terasaki et al. (2019). To be consistent with our modeling, we have refitted the mixing model of Terasaki et al. (2019) to their experimental data by using the EOS of Komabayashi (2014) for pure liquid Fe. Details of the mixing models and the fitting procedure are provided in Text D of supporting information.

#### 2.4. Modeling the Interior Structure of Mercury

Spherically uniform interior structure models of Mercury's interior are computed that are consistent with Mercury's mass, moment of inertia ( $I$ ) and the moment of inertia of its outer solid silicate shell ( $I_m$ ). The polar moment of inertia of Mercury ( $C$ ) and that of its outer solid shell ( $C_m$ ) are expressed in terms of Mercury's obliquity ( $\theta = 2.04 \pm 0.08$  arcmin, Margot et al., 2012), the amplitude of Mercury's forced librations in longitude ( $\psi = 38.5 \pm 1.6$  arcsec, Margot et al., 2012) and the second-degree gravity harmonics  $C_{20}$  and  $C_{22}$  ( $-5.0317 \times 10^{-5}$  and  $8.0399 \times 10^{-6}$ , respectively, Konopliv et al., 2020) by Peale's equations (Peale, 1981; and Equations E13 and E14 of supporting information). From the small (1.96 arcmin), central (2.04 arcmin), and large (2.12 arcmin) values of the  $\pm$  uncertainty margins on  $\theta$ , we obtain values for  $C$  of 0.3323 MR<sup>2</sup> (small), 0.3458 MR<sup>2</sup> (central), and 0.3593 MR<sup>2</sup> (large), respectively. These values overlap with the  $C$ -values computed with the obliquities of Mercury measured by Mazarico et al. (2014), Stark et al. (2015), Genova et al. (2019), and Konopliv et al. (2020; by private communication with their corresponding author is confirmed that their obliquity should be 2.04 arcmin, as calculated from their right ascension and declination). The  $C$  of  $0.333 \pm 0.005$  MR<sup>2</sup> estimated from Genova et al. (2019)'s measurement of the obliquity of Mercury's gravity field is near the small  $C$  that is computed here. From the small (36.9 arcsec), central (38.5 arcsec), and large (40.1 arcsec) values that correspond to the  $\pm$  uncertainty margins on  $\psi$ , we obtain  $C_m$  of 0.1539 MR<sup>2</sup> (large), 0.1475 MR<sup>2</sup> (central), and 0.1416 MR<sup>2</sup> (small), respectively. Because this study considers spherically uniform interior structure models of Mercury, no distinction is made between the principal moments of inertia. Accordingly, interior structure models are computed with  $I$  and  $I_m$  equal to the small, central, and large values of Mercury's polar moment of inertia ( $I = C$ ) and that of its outer solid shell ( $I_m = C_m$ ). This neglect of Mercury's oblateness propagates to an error of  $(2/3)C_{20}MR^2$  on  $I$  (0.0097%) and on  $I_m$  (0.023%).

Peale's equations for  $C$  and  $C_m$  assume that Mercury is in a Cassini state 1. This is verified observationally up to the present-day measurement uncertainties of Mercury's spin axis (e.g., Genova et al., 2019; Margot et al., 2012). Peale's equations do not account for a coupling between the core and the outer solid shell, which can affect the obliquity and the amplitude of forced librations in longitude of Mercury's surface (Peale et al., 2016; Rivoldini & Van Hoolst, 2013; Van Hoolst et al., 2012). Implications of a coupling between the core and the outer solid shell to the interior structure models of this study are discussed in the results section.

A stepped density profile for the crust and the mantle is used to model the outer solid shell of Mercury. The Si-concentration of the inner solid core (if present) is assumed equal (in wt%) to the Si-content of the liquid core, based on the limited fractionation of Si between solid and liquid Fe-rich metal at high pressure (e.g., Kuwayama & Hirose, 2004). Interior structure models are calculated with 0 wt% C, 1.5 wt% C, 3 wt%, or 4.5 wt% C in the liquid core. The composition of the Fe-Fe<sub>3</sub>C eutectic varies from Fe-4 wt% C to Fe-3 wt% C within the 5 GPa to ~35 GPa pressure range of Mercury's core (Fei & Brosh, 2014). Based on melting experiments in the Fe-C system (Fei & Brosh, 2014), the C content of the solid inner core is set to one-third of that in the liquid core in interior structure models with 1.5 wt% C and 3 wt% C in the core liquid (at the Fe-rich side of the Fe-Fe<sub>3</sub>C eutectic). For interior structure models with 4.5 wt% C (at the C-rich side of the Fe-Fe<sub>3</sub>C eutectic), we assume that the solid inner core also contains 4.5 wt% C. Interior structure models

with these amounts of C in the core are also constructed with additional 2 wt% S in the liquid outer core, which does not take part in the solid inner core. For purposes of comparison, interior structure models are also performed with a binary Fe-S liquid outer core and Fe inner core. The density profile of the liquid core is characterized by the FESIC mixing model of Fe-Si-C liquid metals as described in this study. The FESIC model is enhanced by mixing with S using mixing relations that are identified in the Fe-S system by Terasaki et al. (2019) (Text D of supporting information). The phase diagram and density of solid Fe-Si-C is not well understood. For example, Fischer et al. (2013) obtained a mixture of fcc and B2 phases for solid binary Fe-9 wt% Si at the high temperature and (<40 GPa) pressure range that is relevant for Mercury's core. They do not provide an EOS for the density of such mixture, because the obtained phases differ in density by about 3%. In this study, the density profile of the inner core (if present) is characterized by an Fe-Si-C ideal solid mixing model with solid fcc Fe (Komabayashi et al., 2014), Fe<sub>3</sub>C (Litasov et al., 2013), and DO<sub>3</sub> Fe-16 wt% Si (Fischer et al., 2012) endmembers.

Based on thermal evolution studies of Mercury (e.g., Knibbe & van Westrenen, 2018), and supported by the deep dynamo explanation of Mercury's magnetic field (e.g., Christensen, 2006), the interior structure models assume a conductive state for an upper region of Mercury's core. The temperature in this upper part of the core is modeled linear with respect to radius. The conductive temperature gradient is dictated by an assumed thermal conductivity of  $41 \text{ W} \cdot \text{m}^{-1} \cdot \text{K}^{-1}$  (Silber et al., 2018) and heat fluxes of  $5 \text{ mW} \cdot \text{m}^{-2}$  or  $12 \text{ mW} \cdot \text{m}^{-2}$ . These fluxes reflect lower and maximum values of present-day core-mantle boundary (CMB) fluxes obtained from thermal evolution modeling by Knibbe and van Westrenen (2018). Temperatures follow a parametrized adiabat in the deeper region of the core. The transition between the conductive and adiabatic profile is set at the radius where the gradient of the conductive temperature profile equals the gradient of the adiabatic profile. The temperature at the CMB is set at 100 K intervals between 1650 K and 2250 K. The lowest (1650 K) CMB temperature is based on thermal evolution models of Michel et al. (2013). The highest CMB temperature of 2250 K is  $\sim 100 \text{ K}$  hotter than the hottest end-state of Knibbe and van Westrenen (2018)'s thermal evolution scenarios and is considered here for examination purposes. Parametrization of the liquidus temperature for liquid core alloy is based on Morard et al. (2011), Anzellini et al. (2013), Fei and Brosh (2014), and Dumberry and Rivoldini (2015). The location of the inner-core boundary is defined as the crossing between the liquidus and the core's temperature profile.

Details of the interior structure modeling are provided in Text E of supporting information.

### 3. Results

#### 3.1. Experimental Results

Results of experimental density and  $V_P$  measurements are listed in Tables 1 and 2 and plotted with comparison to the values predicted by the FESIC model in Figure 1.

The composition of the recovered samples from the density measurements ranges from binary Fe-15.8 wt% Si to ternary Fe-4.5 wt% Si-4.6 wt% C (Table 1). These compositions are in line with the decreasing solubility of C in Fe-rich metals with increasing Si-concentrations from  $\sim 6 \text{ wt\% C}$  in pure Fe (Dasgupta and Walker, 2008; determined from experiments at 2273–2683 K and 2 GPa) to  $\sim 1 \text{ wt\% C}$  solubility in liquid Fe-17 wt% Si at 5 GPa (Li et al., 2016; Steenstra et al., 2020; Vander Kaaden et al., 2020). The measured densities range from  $5.9\text{--}6.3 \text{ g} \cdot \text{cm}^{-3}$  of liquid Fe-15.8 wt% Si to  $6.77\text{--}6.89 \text{ g} \cdot \text{cm}^{-3}$  of liquid Fe-4.5 wt% Si-4.6 wt% C and Fe-7.2 wt% Si-3.6 wt% C alloys. The measurement errors (between  $\pm 0.21$  and  $\pm 0.24 \text{ g} \cdot \text{cm}^{-3}$ ) are obtained by propagating the measurement errors of the hydrostatic weighing of recovered samples and the uncertainties that are related to fitting the Beer-Lambert law of X-ray absorption to the obtained X-ray absorption profiles (Section A5 of supporting information). The measurement errors are of similar magnitude as the density variations that are induced by compression ( $\sim 0.2 \text{ g} \cdot \text{cm}^{-3}$ , estimated from the EOS of pure Fe liquid from Komabayashi (2014) at 1800 K) and thermal expansion ( $\sim 0.25 \text{ g} \cdot \text{cm}^{-3}$ , estimated from the EOS of pure Fe liquid from Komabayashi (2014) at 4 GPa) in the 3.2–5.9 GPa pressure domain and 1607–2012 K temperature domain spanned by the experiments. As a result, density variations that result from temperature and pressure effects cannot be derived from these density measurements alone.

**Table 1**

Summary of In Situ Density Measurements at ESRF, With the Estimated or Assumed Measured Standard Error Provided in Brackets

Name	$X_{Si}$ (wt%) <sup>a</sup>	$X_C$ (wt%) <sup>a</sup>	$P$ (GPa) <sup>b</sup>	$T$ (K) <sup>b</sup>	$\rho_{S,0}$ (g·cm <sup>-3</sup> ) <sup>c</sup>	$\rho_{S,0}\mu_S$ (m <sup>-1</sup> ) <sup>c</sup>	$\rho_{S,PT}\mu_S$ (m <sup>-1</sup> ) <sup>c</sup>	$\rho_{S,PT}$ (g·cm <sup>-3</sup> ) <sup>c</sup>	FESIC model (g·cm <sup>-3</sup> ) <sup>d</sup>
Exp1	7.2 (0.8)	3.6 (0.3)	3.27 (0.5)	1607 (150)	7.17 (0.10)	3,895 (78)	3,678 (74)	6.77 (0.21)	6.71
Exp2	7.2 (0.8)	3.6 (0.3)	4.18 (0.5)	1748 (150)	7.17 (0.10)	3,895 (78)	3,724 (74)	6.85 (0.22)	6.70
Exp4	7.2 (0.8)	3.6 (0.3)	5.89 (0.5)	1869 (150)	7.17 (0.10)	3,895 (78)	3,747 (75)	6.89 (0.22)	6.75
Exp5	15.8 (0.4)	0 (<0.38)	3.92 (0.5)	1984 (150)	6.53 (0.18)	3,508 (70)	3,263 (65)	6.07 (0.24)	6.20
Exp6	15.8 (0.4)	0 (<0.38)	4.71 (0.5)	1908 (150)	6.53 (0.18)	3,508 (70)	3,202 (64)	5.96 (0.23)	6.28
Exp7	15.8 (0.4)	0 (<0.38)	5.59 (0.5)	1999 (150)	6.53 (0.18)	3,508 (70)	3,387 (68)	6.30 (0.25)	6.30
Exp8	13.6 (1.1)	0.6 (0.9)	3.36 (0.5)	1901 (150)	6.86 (0.15)	3,588 (72)	3,254 (65)	6.23 (0.22)	6.31
Exp9	13.6 (1.1)	0.6 (0.9)	4.23 (0.5)	2012 (150)	6.86 (0.15)	3,588 (72)	3,371 (67)	6.45 (0.23)	6.31
Exp11	4.5 (0.7)	4.6 (0.5)	3.92 (0.5)	1984 (150)	7.34 (0.10)	4,091 (82)	3,777 (76)	6.77 (0.21)	6.71
Exp12	13.6 (1.1)	0.6 (0.9)	5.78 (0.5)	1972 (150)	6.86 (0.15)	3,588 (72)	3,517 (70)	6.73 (0.24)	6.43
Exp13	4.5 (0.7)	4.6 (0.5)	4.23 (0.5)	1906 (150)	7.34 (0.10)	4,091 (82)	3,840 (77)	6.89 (0.22)	6.76

Abbreviations: BN, boron-nitride; EOS, equation of state; ESRF, European Synchrotron Radiation Facility.

<sup>a</sup>Composition of Run Products From Microprobe analysis. The standard errors are dominated by the variability in microprobe spot analyses (Text B of supporting information). <sup>b</sup>Pressure and temperature conditions determined from isochore crossings of Pt and BN EOSs using in situ measured unit-cell volumes of corresponding calibrants. The standard errors are based on uncertainties in the EOSs for Pt and BN (Table A3 of supporting information).

<sup>c</sup>Results from hydrostatic weighing and X-ray absorption measurements (Tables A1 and A2 of supporting information). Standard errors are estimated from the precision of the high-precision balance that is used for hydrostatic weighing and the propagation of uncertainties that are inherent to modeling the X-ray absorption data (Section A5 of supporting information). <sup>d</sup>The FESIC model value at corresponding composition and pressure and temperature conditions.

The densities predicted by the FESIC ternary ideal mixing model (Text D of supporting information) are within the 1 sigma error bars of all-but-two density measurements (Figure 1, right). The predicted densities are 0.09 g·cm<sup>-3</sup> above the measurement's error margin of Exp6 on Fe-15.8 wt% Si and 0.06 g·cm<sup>-3</sup> below the measurement's error margin of Exp12 on Fe-13.6 wt% Si-0.6 wt% C. This difference may be related to uncertainties in experimental temperature conditions ( $\pm 150$  K), pressure conditions ( $\pm 0.5$  GPa), and sample composition (Table 1), which are not incorporated in the reported measurement errors. For example, the densities of the FESIC model at temperature 150 K higher for Exp6 and 150 K lower for Exp12 would be within the reported error margins of the corresponding density measurements.

The compositions of the recovered samples from the two ultrasonic measurements FeSi10 and FeSi17 are measured by electron microprobe at Fe-10.8 wt% Si-0.82 wt% C and Fe-16.9 wt% Si, respectively. The measured concentration of C of these samples (below microprobe detection limit for the FeSi17 sample) is below the C-solubility limit (e.g., Li et al., 2016; Steenstra et al., 2020; Vander Kaaden et al., 2020). The sample in the ultrasonic assembly is not in direct contact with C-rich material (see Figure C1 of supporting information for a schematic layout of the assembly). The carbon that is detected in the FeSi10 sample is possibly of environmental origin (e.g., Kuwahara et al., 2019).

The measured  $V_p$  ranges from  $4,243 \pm 62$  m·s<sup>-1</sup> on FeSi10 at 1752 K and 2.2 GPa to  $4,701 \pm 71$  m·s<sup>-1</sup> measured on FeSi17 at 1549 K and 4.32 GPa (Figure 1, Table 2). The three highest  $V_p$  measurements on FeSi17 (4,668–4,704 m·s<sup>-1</sup> at 3.52–4.32 GPa) are considerably higher than those obtained by FeSi17 at lower pressure (4,364–4,478 m·s<sup>-1</sup> at 2.12–2.98 GPa). The  $V_p$  of the FESIC model yields a  $V_p$  slightly below the measurement error margins for two of these  $V_p$  measurements (FeSi17\_7 and FeSi17\_8) at between 3.5 GPa and 3.7 GPa (Figure 1, table 2). For the measurements FeSi17\_7 (3.52 GPa) and FeSi17\_9 (4.32 GPa), the parametrized liquidus temperature of the alloy (Fe-16.9 wt% Si) is 30° higher and 79° higher, respectively, than the experimental temperatures that are determined by the isochore-crossings of BN-Al<sub>2</sub>O<sub>3</sub>. This might suggest that the sample was not fully molten during the measurements at >3.5 GPa, which could explain

**Table 2**

*Summary of In Situ  $V_P$  Measurements at APS, With the Estimated or Assumed Measured Standard Error Provided in Brackets*

Name	$X_{Si}$ (wt%) <sup>a</sup>	$X_C$ (wt%) <sup>a</sup>	$P$ (GPa) <sup>b</sup>	$T$ (K) <sup>b</sup>	$D$ ( $10^{-4}$ m) <sup>c</sup>	$\theta$ ( $10^{-7}$ s) <sup>c</sup>	$V_P$ (m/s) <sup>c</sup>	FESIC model (m/s) <sup>d</sup>
FeSi10_1	10.7 (0.3)	0.8 (0.2)	2.20 (0.5)	1752 (150)	3.688 (0.03)	1.739 (0.01)	4,241 (42)	4,267
FeSi10_2	10.7 (0.3)	0.8 (0.2)	2.91 (0.5)	1627 (150)	2.832 (0.03)	1.289 (0.01)	4,394 (58)	4,389
FeSi10_3	10.7 (0.3)	0.8 (0.2)	3.21 (0.5)	1576 (150)	2.518 (0.03)	1.161 (0.01)	4,337 (64)	4,438
FeSi17_1	16.9 (0.4)	0 (<0.2)	2.12 (0.5)	1564 (150)	4.241 (0.03)	1.943 (0.01)	4,366 (38)	4,433
FeSi17_2	16.9 (0.4)	0 (<0.2)	2.16 (0.5)	1617 (150)	4.037 (0.03)	1.840 (0.01)	4,389 (40)	4,414
FeSi17_3	16.9 (0.4)	0 (<0.2)	2.52 (0.5)	1581 (150)	3.715 (0.03)	1.681 (0.01)	4,420 (44)	4,466
FeSi17_4	16.9 (0.4)	0 (<0.2)	2.65 (0.5)	1644 (150)	3.642 (0.03)	1.655 (0.01)	4,403 (45)	4,452
FeSi17_5	16.9 (0.4)	0 (<0.2)	2.91 (0.5)	1531 (150)	3.393 (0.03)	1.518 (0.01)	4,470 (49)	4,525
FeSi17_6	16.9 (0.4)	0 (<0.2)	2.98 (0.5)	1579 (150)	3.325 (0.03)	1.485 (0.01)	4,478 (50)	4,511
FeSi17_7	16.9 (0.4)	0 (<0.2)	3.52 (0.5)	1563 (150)	3.074 (0.03)	1.320 (0.01)	4,657 (58)	4,570
FeSi17_8	16.9 (0.4)	0 (<0.2)	3.61 (0.5)	1623 (150)	2.988 (0.03)	1.275 (0.01)	4,687 (60)	4,554
FeSi17_9	16.9 (0.4)	0 (<0.2)	4.32 (0.5)	1549 (150)	2.545 (0.03)	1.082 (0.01)	4,704 (71)	4,648

Abbreviations: APS, Advanced Photon Source; BN, boron-nitride; EOS, equation of state.

<sup>a</sup>Run product composition from microprobe analysis. The standard errors are dominated by the variability in microprobe spot analyses (Text B of supporting information). <sup>b</sup>Pressure and temperature conditions determined from isochore crossings of  $Al_2O_3$  and BN EOSs using in situ measured unit-cell volumes of corresponding calibrants. Standard errors are based on uncertainties in the EOSs of  $Al_2O_3$  and BN (Table C1 of supporting information). <sup>c</sup>Results of radiographic imaging and ultrasonic measurements (Table C1 of supporting information). Standard errors are estimated from the propagation of uncertainties that are inherent to fitting the ultrasonic data and the radiographic image data (Section C4 of supporting information). <sup>d</sup>The FESIC model value at corresponding composition and pressure and temperature conditions.

the significantly higher  $V_P$  that is measured. Nevertheless, the FeSi17\_8  $V_P$  measurement at 3.61 GPa has an estimated experimental temperature that exceeds the parametrized liquidus with 23 degrees and yields a similar  $V_P$  to the FeSi17\_7 and FeSi17\_9 measurements. Moreover, the in situ X-ray spectra that are collected directly prior to the ultrasonic measurements do not reveal any crystalline features, indicating that the sample was molten at least to a large extent during the ultrasonic measurements. It is therefore more likely that the parametrization of the liquidus is several tens of degrees overestimated for this alloy or that the experimental temperature, which is determined with an expected  $\pm 150$  K uncertainty, is underestimated for the  $V_P$  measurements that are performed at  $>3.5$  GPa.

An additional model for the liquid alloy (hereafter referred to as the FESIC\_LP model) that excludes the  $V_P$  measurements that are performed at  $>3.5$  GPa in the parameter fitting is developed analogously to the FESIC model. This model examines implications of the possibility that an incompletely molten state of the sample has affected the  $V_P$  measurements that are performed at  $>3.5$  GPa. In general, the FESIC\_LP model yields a lower  $V_P$  than the FESIC model, of which the difference increases with increasing pressure (Figure 1, left). The densities of the FESIC and FESIC\_LP models are practically indistinguishable in the pressure range of  $<5.8$  GPa that is experimentally investigated here (Figure 1, right).

### 3.2. Comparison to Literature Data

In Figure 2, FESIC model densities are compared to density measurements on related liquid Fe-rich alloys at pressures up to 12 GPa that are reported in literature (Sanloup et al., 2004; Tateyama et al., 2011; Terasaki et al., 2019; Yu & Secco, 2008).



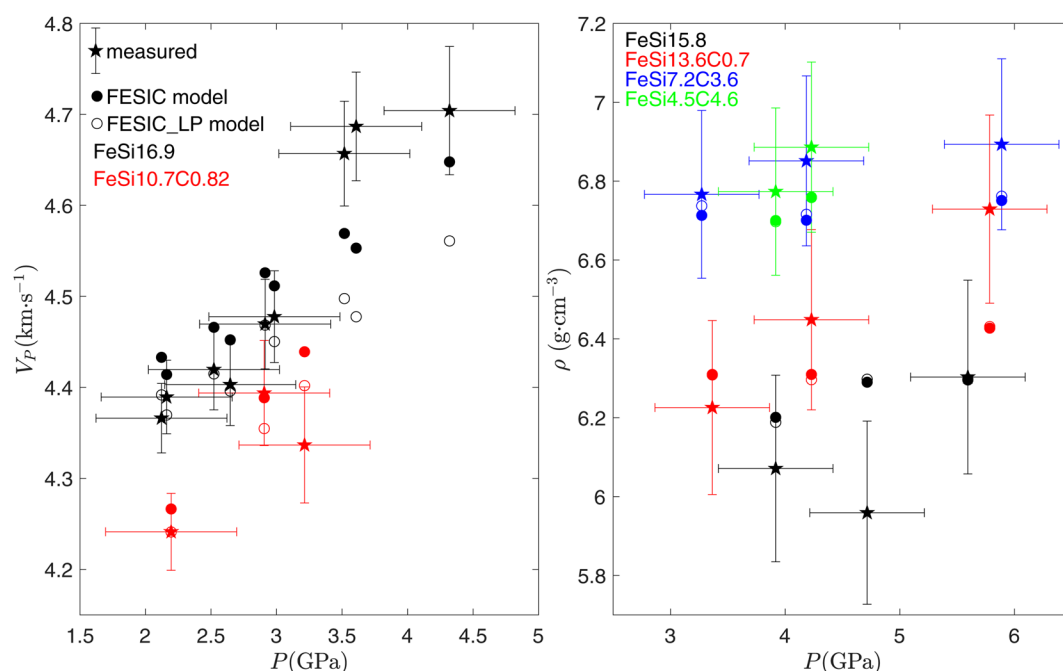


**Figure 1.** Experimental  $V_p$  (left) and density (right) measurements of this study (pentagrams, see Tables 1 and 2) and the predicted model values of the FESIC (filled circles) and FESIC\_LP (open circles) ideal ternary mixing models. The sample compositions denoted by FeSiXCY correspond to measurements on Fe-X wt% Si-Y wt% C samples (Tables 1 and 2). Estimated experimental temperatures range from 1531 K to 1751 K for the  $V_p$  measurements (left) and from 1607 K to 1012 K for the density measurements (right). Standard errors on  $V_p$  result from the propagation of uncertainties that are inherent to fitting the ultrasonic data and modeling of the radiographic image data (Section C4 of supporting information). Standard errors on density are estimated from the precision of the high-precision balance that is used for hydrostatic weighing and the propagation of uncertainties that are inherent to modeling the X-ray absorption data (Section A5 of supporting information). Standard errors on pressure of 0.5 GPa are based on the uncertainties on EOSs of the pressure and temperature calibrants BN and Al<sub>2</sub>O<sub>3</sub> (Dubrovinski et al., 1998; Wakabayashi & Funamori, 2015) for the  $V_p$  measurements and BN and Pt (Fei et al., 2007; Wakabayashi & Funamori, 2015) for the density measurements. BN, boron-nitride; EOS, equation of state.

Yu and Secco (2008) reported sink-float density measurements of liquid Fe-17 wt% Si that are performed at pressures up to 12 GPa. The FESIC mixing model matches the neutrally buoyant measurements of Yu and Secco (2008) to within measurement error ( $\pm 0.3$  g·cm<sup>-3</sup>).

Terasaki et al. (2019) reported density measurements of liquid Fe-16.9 wt% Si-10 wt% Ni and of liquid Fe-23.4 wt% Si-10 wt% Ni that are performed at pressures between 2.5 GPa and 4.5 GPa by X-ray absorption techniques similar to those used in this study. They developed a nonideal Fe-Si mixing model that matches their density measurements to within the small reported formal measurement errors of between 0.03 g·cm<sup>-3</sup> and 0.06 g·cm<sup>-3</sup>. Our ideal FESIC mixing model yields on average 0.09 g·cm<sup>-3</sup> (largest difference is 0.15 g·cm<sup>-3</sup>) lower densities than measured by Terasaki et al. (2019). Most densities of the FESIC model are slightly outside the small error margins reported by Terasaki et al. (2019). The 10 wt% Ni that is present in Terasaki et al. (2019)'s samples can explain a 0.05 g·cm<sup>-3</sup> higher density measured by Terasaki et al. (2019) compared to the Ni-free alloys modeled by the FESIC model (Watanabe et al., 2016). For many of the measurements of Terasaki et al. (2019), this influence of Ni does not resolve the observed density difference with the FESIC model with respect to the small error margins reported by Terasaki et al. (2019). However, a significant uncertainty ( $>2\%$ ) in X-ray absorption density measurements is associated with modeling assumptions of the X-ray absorption profiles (Section A5 of supporting information). Such uncertainties are not incorporated in the error margins reported by Terasaki et al. (2019). If only half of the error margins that are used in this study are adopted for the measurements by Terasaki et al. (2019), the FESIC model is within the error relative to all density measurements of Terasaki et al. (2019) if the influence of Ni is taken into account.

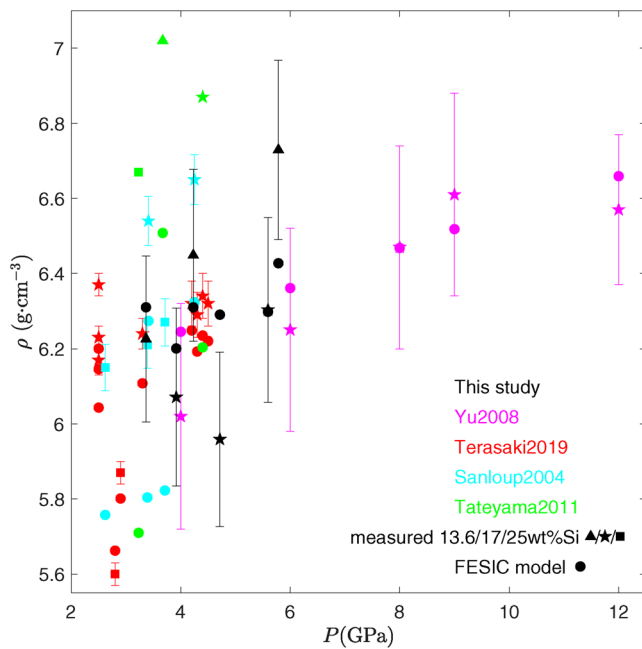


**Figure 2.** Model values of the FESIC ternary mixing model (filled circles) at pressure and temperature conditions and of composition corresponding to literature density measurements of Sanloup et al. (2004, cyan), Yu and Secco (2008, magenta), Tateyama et al. (2011, green), and Terasaki et al. (2019, red). Density measurements of this study of Fe-16.9 wt% Si and Fe-13.6 wt% Si-0.6 wt% C are also plotted (black). Triangle, pentagram and square symbols represent binary Fe-Si alloys with Si concentrations of 13.6 wt%, 17 wt%, and 25 wt%, respectively. Exceptions are the measurements of Terasaki et al. (2019) performed on Fe-16.9 wt% Si-10 wt% Ni (pentagrams) and Fe-23.4 wt% Si-10 wt% Ni (squares), for which the FESIC model is evaluated at Fe-16.9 wt% Si and Fe-23.4 wt% Si, respectively. An additional exception is a measurement on Fe-11 wt% Si by Tateyama et al. (2011), which is plotted with green triangle symbol. The FESIC\_LP model (not plotted) has densities very similar to those of the FESIC model in the pressure range of this figure.

Sanloup et al. (2004) reported density measurements of liquid Fe-17 wt% Si and of liquid Fe-25 wt% Si that are performed at pressures between 0.8 GPa and 4.5 GPa by X-ray absorption techniques similar to those used in this study. Their reported density measurements are between  $0.21 \text{ g}\cdot\text{cm}^{-3}$  higher and  $0.40 \text{ g}\cdot\text{cm}^{-3}$  higher than the densities predicted by the FESIC model. Sanloup et al. (2004) report a precision of the measured density ( $\rho$ ) of 1% ( $\sim 0.06 \text{ g}\cdot\text{cm}^{-3}$ ), which is used as  $\pm$  error bar in Figure 1. Sanloup et al. (2004) additionally reported variations of the X-ray mass absorption coefficient ( $\mu$ ) of 2.5% ( $\sim 0.16 \text{ g}\cdot\text{cm}^{-3}$ ). This uncertainty is a lower boundary of the actual uncertainty on  $\rho$ , because the multiplication of the two ( $\mu\rho$ ) is inferred by the analysis of X-ray absorption profiles. In light of other potential measurement errors related to using different pressure and temperature calibration, compositional uncertainties, and other methodological uncertainties, it may be possible that the actual error margins on some of the density measurements of Sanloup et al. (2004) overlap with the FESIC model.

Tateyama et al. (2011) reported sink-float density measurements of liquid Fe-11 wt% Si, Fe-17 wt% Si, and Fe-25 wt% Si at 4 GPa. These density measurements are between  $0.36 \text{ g}\cdot\text{cm}^{-3}$  and  $0.97 \text{ g}\cdot\text{cm}^{-3}$  higher than corresponding values of the FESIC model. We cannot explain the large deviation of the density measurements reported by Tateyama et al. (2011).

To summarize, the near-binary Fe-Si density measurements of this study (Exp5, Exp6, Exp7, Exp8, Exp9, and Exp12) are in line with density measurements of Terasaki et al. (2019) and Yu and Secco (2008). The results indicate that Si reduces the density of liquid Fe-rich metals more strongly than indicated by experimental measurements reported by Sanloup et al. (2004) and, particularly, by Tateyama et al. (2011).

The  $V_P$  measurements of liquid Fe-16.9 wt% Si performed in this study yield  $\sim 100 \text{ m}\cdot\text{s}^{-1}$  higher velocities than measured by Terasaki et al. (2019) on Fe-16.9 wt% Si-10 wt% Ni at  $\sim 150 \text{ K}$  higher temperatures in a pressure range similar to that experimentally explored in this study (Figure 3, left panel). Ambient pressure  $V_P$  measurements of Williams et al. (2015) yield a temperature derivative of  $V_P$  ( $\delta V_P / \delta T$ ) of between  $-0.33 \text{ m}\cdot\text{s}^{-1}\cdot\text{K}^{-1}$  and  $-0.5 \text{ m}\cdot\text{s}^{-1}\cdot\text{K}^{-1}$  for similar liquid alloy (Fe-(6-20) wt% Si-5 wt% Ni)

(see Figure D1 of supporting information). This relation between temperature and  $V_P$  accounts for the difference between  $V_P$  measurements by Terasaki et al. (2019) and this study. The FESIC model, for which the measurements of Williams et al. (2015) are included in the parameter fitting, indeed matches the majority of Terasaki et al. (2019)'s  $V_P$  measurements to within the reported error margins (Figure 3, left and upper right panels). However, the FESIC\_LP model, for which the three  $V_P$  measurements at  $>3.5 \text{ GPa}$  are excluded in the parameter fitting, yields a  $V_P$  that is significantly lower than measured by Terasaki et al. (2019) at pressures above  $\sim 3 \text{ GPa}$ . We conclude that the FESIC ideal mixing model is in good agreement with the  $V_P$  measurements performed at pressures up to 12 GPa on Fe-16.9 wt% Si-10 wt% Ni and Fe-23.5 wt% Si-10 wt% Ni by Terasaki et al. (2019). This indicates that nonideal mixing of Fe-rich liquid metal with Si may not be required to match their density and  $V_P$  measurements to within experimental uncertainties. The FESIC\_LP model yields significantly lower  $V_P$  than measured by Terasaki et al. (2019) (Figure 3, left and upper right panels).

The  $\delta V_P / \delta T$  between  $-0.33 \text{ m}\cdot\text{s}^{-1}\cdot\text{K}^{-1}$  and  $-0.5 \text{ m}\cdot\text{s}^{-1}\cdot\text{K}^{-1}$  obtained by Williams et al. (2015; see Figure D1 of supporting information) indicates that the compressibility of Si-containing Fe-rich metallic liquid increases with temperature. At between 30 GPa and 100 GPa and an average temperature of 2800 K, Morard et al. (2013) measured densities on liquid Fe-15 wt% Si-5 wt% Ni samples that increase with increasing pressure from  $6.9 \text{ g}\cdot\text{cm}^{-3}$  to  $7.8 \text{ g}\cdot\text{cm}^{-3}$  (Figure 3, lower right panel). These densities are on the low side to be

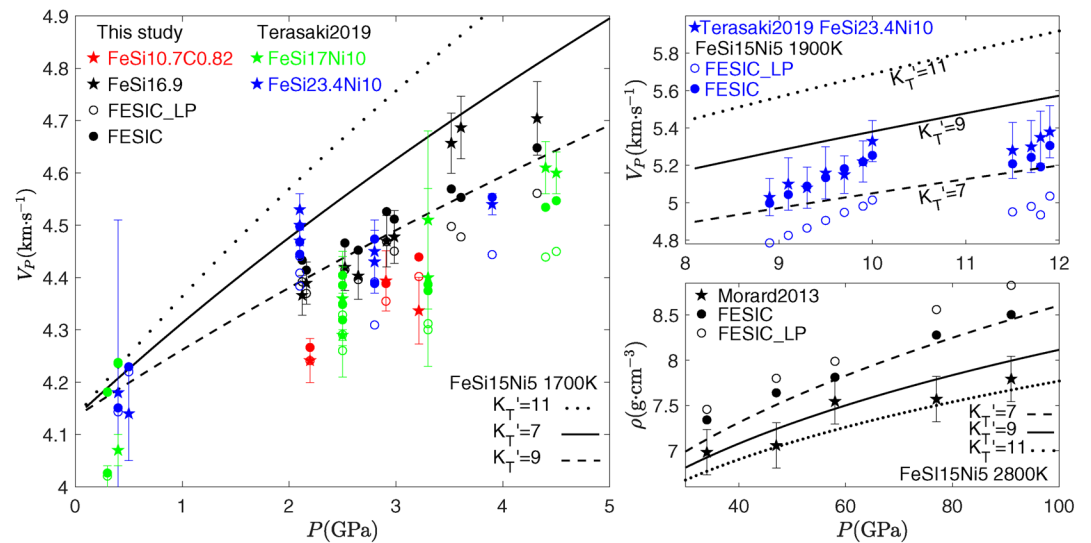


**Figure 3.** Comparison of  $V_p$  measurements (pentagrams) and the FESIC (filled circle) and FESIC\_LP (open circle) mixing models to  $V_p$  and density measurements from literature. (left and upper right) High pressure  $V_p$  measurements of this study (black for liquid Fe-16.9 wt% Si and red for liquid Fe-10.7 wt% Si-0.82 wt% C) and of Terasaki et al. (2019, green for liquid Fe-17 wt% Si-10 wt% Ni and blue for liquid Fe-23.4 wt% Si-10 wt% Ni). Average temperature of the  $V_p$  measurements of this study is 1606 K. Average experimental temperatures of Terasaki et al. (2019) are 1853 K for the  $V_p$  measurements plotted in the left panel and 1874 K for the  $V_p$  measurements in the upper right panel. (lower right) High-pressure density measurements of Morard et al. (2013) of liquid Fe-15 wt% Si-5 wt% Ni. (general) Dotted, solid and dashed lines represent EOSs of Fe-15 wt% Si-5 wt% Ni (see Table D1 of supporting information) with  $K_T'$  ( $\delta K_T' / \delta P$  at ambient pressures) of 11, 9, and 7, respectively. These lines are evaluated at 1700 K in the left panel, at 1900 K in the upper right panel, and at 2800 K in the lower right panel. Model values of the FESIC (filled circle) and FESIC\_LP (open circle) ternary mixing models are evaluated at pressure and temperature conditions that correspond to the plotted literature measurements. For comparison to ternary Fe-X wt% Si-Y wt% Ni measurements, the FESIC and FESIC\_LP models are evaluated at corresponding Fe-X wt% Si composition.

consistent with the small  $K_T'$  of between 30 GPa and 50 GPa at 2800 K at ambient pressure that follows from the  $\delta V_p / \delta T$  determined by Williams et al. (2015). Williams et al. (2015) reconcile these measurements by predicting that the compressibility of Fe-Si liquids strongly decreases with pressure, that is, they predict a large pressure derivative of the bulk modulus  $K_T'$  at ambient pressure ( $\delta K_T' / \delta P$ ) of between 9 and 12.5 for Fe-15 wt% Si-5 wt% Ni. Figure 3 shows densities computed by a Vinet EOS for Fe-15 wt% Si-5 wt% Ni alloy under model assumptions similar to those of Williams et al. (2015) that are consistent with their  $V_p$  measurements using  $K_T'$  of 7, 9 or 11 (Table D1 of supporting information lists all model parameters). The EOSs with high  $K_T'$  of 9 or 11 are within error with respect to Morard et al. (2013)'s density measurements (Figure 3, lower right panel). But our  $V_p$  measurements on Fe-16.9 wt% Si, and also those of Terasaki et al. (2019) on Fe-16.9 wt% Si-10 wt% Ni, are most in line with the EOS with  $K_T'$  of 7. The FESIC model that is fitted to our measurements and to those of Williams et al. (2015) has a  $K_T'$  of 6.55 for Fe-15 wt% Si liquid at ambient pressure. Consequently, the FESIC model yields higher densities than measured by Morard et al. (2013) at their experimental high-pressure high-temperature conditions (Figure 3, lower right panel). The high  $K_T'$  of between 9 and 11 that is required for obtaining densities of liquid Fe-15 wt% Si-5 wt% Ni as low as measured by Morard et al. (2013) is not supported by the  $V_p$  measured on similar alloys in this study and those measured by Terasaki et al. (2019). The FESIC\_LP model has a  $K_T'$  of 5.44 for Fe-15 wt% Si liquid at ambient pressure. Consequently, the FESIC\_LP model is in stronger disagreement with the density measurements at >30 GPa by Morard et al. (2013) compared to the FESIC model (Figure 3, lower right panel).

Density and  $V_p$  measurements on Fe-3.5wt%C by Shimoyama et al. (2016) have been included in the fitting procedure of the FESIC model for calibrating the EOS of the  $\text{Fe}_3\text{C}$  endmember. Figure 4 compares the density and  $V_p$  measurements on binary liquid Fe-C alloys (Nakajima et al., 2015; Shimoyama et al., 2016; Terasaki et al., 2010) to the FESIC model values. The FESIC model is within experimental error to most of the density and  $V_p$  measurements of Shimoyama et al. (2016) and within experimental error to all density

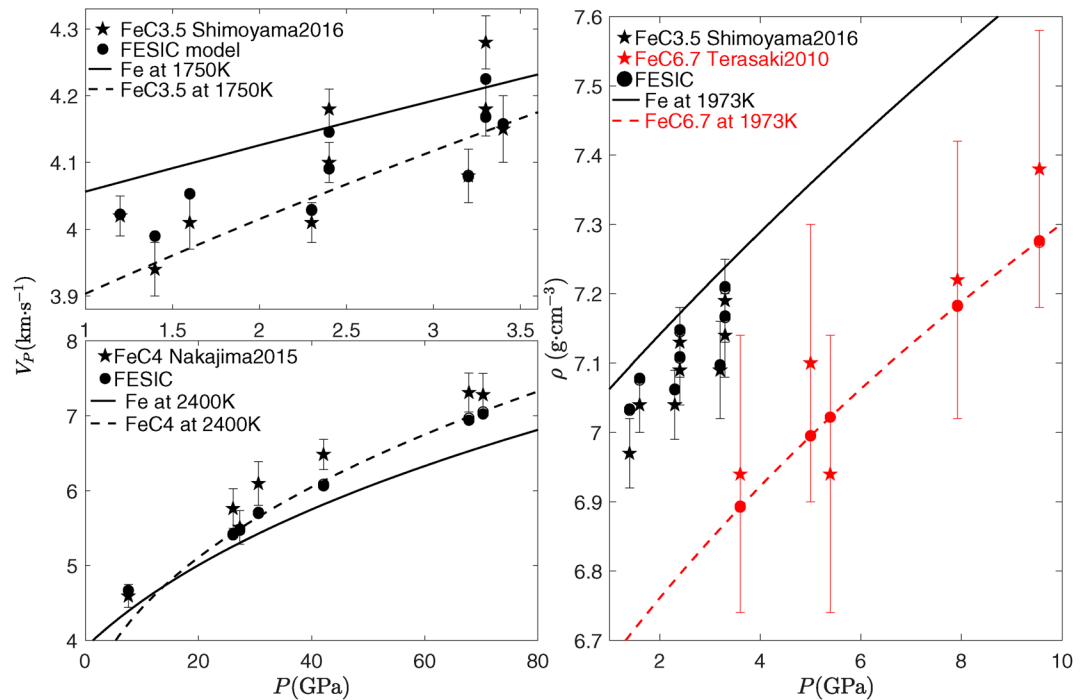


**Figure 4.** High pressure  $V_p$  (left) and density (right) measurements of liquid binary Fe-C mixtures by Shimoyama et al. (2016; of Fe-3.5 wt% C) at average temperature of 1720 K, Terasaki et al. (2010; of Fe-6.7 wt% C, red) at 1973 K and Nakajima et al. (2015; of Fe-4 wt% C) at an average temperature of 2434 K (pentagrams). FESIC model values at pressure and temperature conditions that correspond to the experimental conditions of the literature data are plotted by filled circles. Solid lines represent pure Fe (Komabayashi, 2014) at 1750 K ( $V_p$ , top left), at 2400 K ( $V_p$ , bottom left) and at 1973 K (density, right). Dashed lines represent the FESIC model values at identical temperatures as the solid line for Fe-3.5 wt% C ( $V_p$ , top left), Fe-4 wt% C ( $V_p$ , bottom left), and Fe-6.7wt%C (density, right, in red).

measurements of Terasaki et al. (2010) (Figure 4, right panel). The  $V_p$  of the FESIC model decreases with C-concentration at the <3.5 GPa pressures explored by experiments of Shimoyama et al. (2016) (Figure 4, upper left panel), whereas  $V_p$  increases with increasing concentrations of C at pressure above ~10 GPa (Figure 4, bottom left panel). This property of the FESIC model is consistent with the  $V_p$  measurements on liquid Fe-4wt%C by Nakajima et al. (2015) at high pressures (7–71 GPa), although only half of the measurements by Nakajima et al. (2015) are matched by the FESIC model to within the reported measurements errors. The density measurements of ternary Fe-Si-C alloys of this study that contain significant amounts of C (Exp1, 2, 4, 11, and 13) are matched by the FESIC model to within the measurement errors under the assumption of ideal mixing (Figure 1). The FESIC\_LP model is identical to the FESIC model in the binary Fe-C domain.

We recall that there are no indications in the experimental data analysis that the sample was incompletely molten during the  $V_p$  measurements that are performed at >3.5 GPa. Also, the FESIC model is in better agreement with the available measurements in literature of  $V_p$  (Terasaki et al., 2019) and density (Morard et al., 2013) at high pressures that are relevant for Mercury's core compared to the FESIC\_LP model. For these reasons, we consider the FESIC model as the preferred model for characterizing the liquid outer core of Mercury.

### 3.3. Comparison of Mixing Models

In this section, the mixing behavior of the light elements Si, C, and S with Fe liquid metal, as predicted by the FESIC model and mixing models of Terasaki et al. (2019), is discussed. The  $V_p$  and density of the FESIC model vary almost linearly with (wt%) concentrations of Si and C (Figure 5). At 2000 K,  $\delta V_p / \delta X_C$  increases with pressure from  $\sim -30 \text{ m} \cdot \text{s}^{-1}$  per wt%C at 5 GPa to  $\delta V_p / \delta X_C$  of  $\sim 75 \text{ m} \cdot \text{s}^{-1}$  per wt% C at 35 GPa,

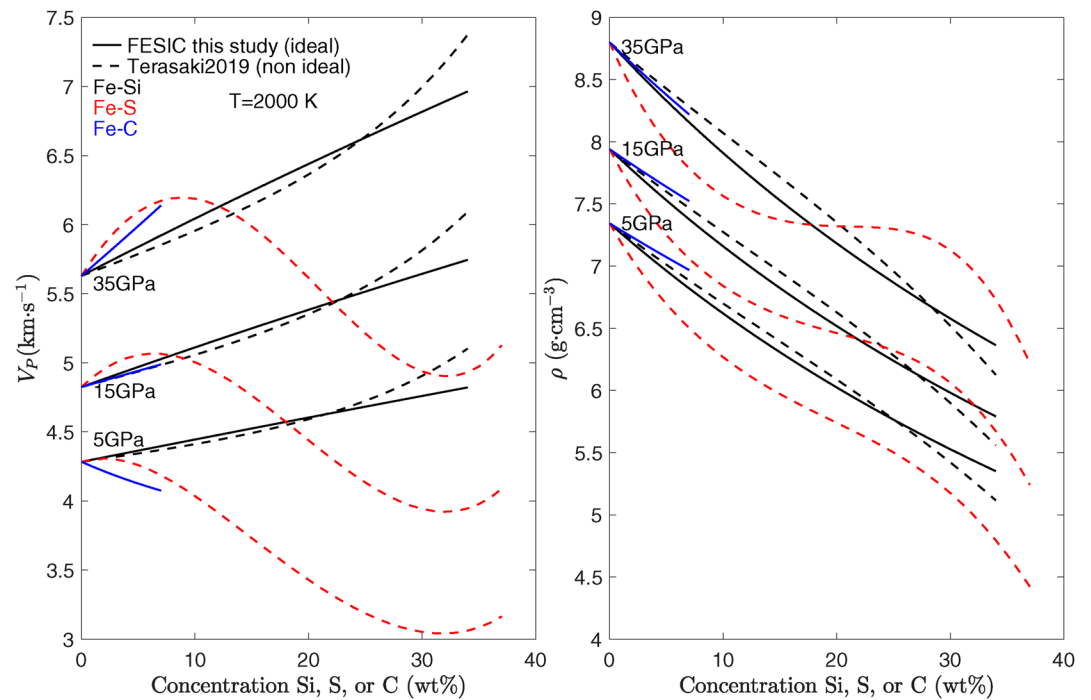


**Figure 5.** Comparison between the  $V_p$  (left) and density (right) for mixing models between Fe-Si (black), Fe-C (blue), and Fe-S (red) at 2000 K. Solid lines represent values according to the FESIC model of this study (ternary Fe-FeSi-Fe<sub>3</sub>C). Dashed lines represent the nonideal mixing models of Terasaki et al. (2019).

and  $\delta\rho / \delta X_C$  decreases with pressure from  $\sim -53 \text{ kg}\cdot\text{m}^{-1}$  per wt% C at 5 GPa to  $\sim -86 \text{ kg}\cdot\text{m}^{-1}$  per wt% C at 35 GPa. The change between a negative  $\delta V_p / \delta X_C$  at low pressure and positive  $\delta V_p / \delta X_C$  at high pressure is in line with the experimental  $V_p$  measurements at low pressures (Shimoyama et al., 2016) and at high pressures (Nakajima et al., 2015; Figure 4). Regarding the Fe-Si mixing, the FESIC model predicts a  $\delta\rho / \delta X_{Si}$  of  $\sim -67 \text{ kg}\cdot\text{m}^{-1}$  per wt% Si that is independent of pressure, whereas  $\delta V_p / \delta X_{Si}$  increases with pressure from  $\sim 16 \text{ m}\cdot\text{s}^{-1}$  per wt% Si at 5 GPa to  $\delta V_p / \delta X_{Si}$  of  $\sim 37 \text{ m}\cdot\text{s}^{-1}$  per wt% Si at 35 GPa. In the binary Fe- $<25$  wt% Si domain, the FESIC model is consistent with the nonideal mixing model of Terasaki et al. (2019) (differences are below  $70 \text{ m}\cdot\text{s}^{-1}$  and below  $0.15 \text{ g}\cdot\text{cm}^{-3}$ ). For Mercury's core, a Si concentration of the core higher than 25 wt% is not expected (e.g., Knibbe & van Westrenen, 2018). Therefore, implementation of either Terasaki et al. (2019)'s nonideal Fe-Si mixing model or the FESIC model in interior structure models will lead to similar inferences about Mercury. For Fe- $(>25$  wt%) Si compositions, Terasaki et al. (2019)'s nonideal mixing model yields up to  $\sim 500 \text{ m}\cdot\text{s}^{-1}$  higher  $V_p$  compared to the FESIC model. Experimental data in this compositional domain is, however, to our knowledge not available at high pressure.

At pressures lower than 5 GPa, the  $V_p$  of Fe-rich metal decreases with increasing concentrations of S (Figure 5). This contrasts with the increasing influence of Si on the  $V_p$  of Fe-rich metal. However, experimental data are indicative of a complex mixing behavior between Fe and S (Morard et al., 2018; Terasaki et al., 2019; Figure 5). According to the nonideal Fe-S mixing model of Terasaki et al. (2019), the  $V_p$  peaks specifically in the 0–10 wt% S domain that is most relevant for Mercury's core, with pressures above  $\sim 5$  GPa. The density of Fe-rich liquid metal decreases strongly with S-concentration in the  $<10$  wt% S and  $>30$  wt% S domains. Density is less sensitive to S in the compositional domain between 10 wt% S and 30 wt% S, according to the nonideal mixing model of Terasaki et al. (2019).



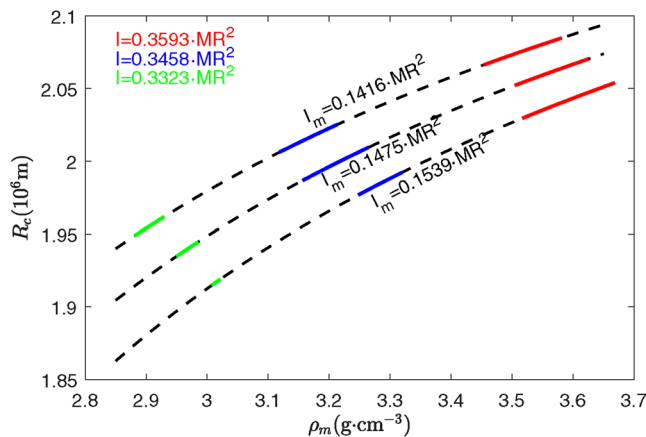


**Figure 6.** The core radius ( $R_c$ ) and mantle density ( $\rho_m$ , i.e., the density of the outer solid shell below the crust-mantle boundary assumed at 2,400 km radius). Dashed lines represent the relation between  $R_c$  and  $\rho_m$  that is controlled by the assumed moment of inertia of the outer solid shell  $I_m$  of 0.1416  $MR^2$ , 0.1475  $MR^2$ , and 0.1539  $MR^2$  of the interior structure models (equation E2 of text E of supporting information). The green, blue and red lines represent the solution space of the interior models of this study with moment of inertia for Mercury  $I$  of 0.3323  $MR^2$ , 0.3458  $MR^2$ , and 0.3593  $MR^2$ , respectively. These values of  $I_m$  and  $I$  equal the small, central and large values of the corresponding polar moments of inertia  $C_m$  and  $C$  calculated by Peale's equations (equations E13 and E14 of text E of supporting information). These values are obtained by propagating the  $\pm$  uncertainty margins on Mercury's obliquity and the amplitude of Mercury's librations in longitude direction reported by Margot et al. (2012).

## 4. Interior Structure Models of Mercury

### 4.1. Presentation of Interior Structure Models of Mercury

The density of the mantle and the radius of the core of the interior structure models are constrained by the moment of inertia ( $I$ ) and that of the outer solid shell ( $I_m$ ; Figure 6). Mercury's core radius varies between 1,915–1,965 km, 1,973–2,025 km, and 2,025–2,080 km, for interior structure models with the small (0.3323  $MR^2$ ), central (0.3458  $MR^2$ ), and large (0.3593  $MR^2$ )  $I$ , respectively. Within these ranges for the core's size constrained by  $I$ , the core radius increases with increasing  $I_m$  from the small value of 0.1416  $MR^2$  to the central value of 0.1475  $MR^2$  and to the large value of 0.1539  $MR^2$  (Figure 6).

The density of the mantle (i.e., the density of the outer solid shell below the crust-mantle boundary that is assumed at 2,400 km radius [Padovan et al., 2015]) is constrained to between 2.88–3.03  $g\cdot cm^{-3}$ , 3.15–3.35  $g\cdot cm^{-3}$ , and 3.43–3.68  $g\cdot cm^{-3}$  for interior structure models with the small (0.3323  $MR^2$ ), central (0.3458  $MR^2$ ), and large (0.3593  $MR^2$ )  $I$  (Figure 6). Within these ranges for the mantle density constrained by  $I$ , the mantle density increases with increasing  $I_m$  (Figure 6).

Geochemical studies indicate that Mercury's mantle is dominated by magnesium (Mg)-rich olivine and pyroxene minerals (e.g., Namur & Charlier, 2017; Namur et al., 2016; Vander Kaaden et al., 2017). The density of Mg-rich olivine and ortho- and clinopyroxene minerals that are proposed for Mercury's mantle ranges between  $\sim 3.11$   $g\cdot cm^{-3}$  and  $\sim 3.26$   $g\cdot cm^{-3}$  (Stixrude & Lithgow-Bertollini, 2011; computed assuming Fe-free compositions). The specific density of the mantle depends on the thermal state of Mercury's mantle and on the specific mineral assemblage (see also Beuthe et al., 2020; Figure S4 of their supporting information).

The interior structure models with the central value of  $I$  thus have a mantle density that is in line with predicted mineral assemblages for Mercury's mantle.

If interior structure models of Mercury with the lower  $I$  are preferred, the density of the mantle must be lowered relative to such Mg-rich mineral assemblages. The mantle density can be lowered by the presence of graphite or calcium (Ca)-rich or Mg-rich sulfides in Mercury's mantle (Boukaré et al., 2019; Malavergne et al., 2014; Vander Kaaden & McCubbin, 2015; Weider et al., 2012). Graphite, CaS and MgS have densities of  $\sim 2.1$   $g\cdot cm^{-3}$ ,  $\sim 2.6$   $g\cdot cm^{-3}$ , and  $\sim 2.7$   $g\cdot cm^{-3}$ , respectively (Peiris et al., 1994; Vander Kaaden & McCubbin, 2015). However, Mercury's surface rocks contain less than 4 wt% S and less than 2.3 wt% C on average (Nittler et al., 2011; Peplowski et al., 2015). Consequently, to substantially lower the mantle's density by graphite or sulfides, these constituents need to be more abundant in the mantle compared to their abundances as measured at Mercury's surface.

If the interior structure models with the large  $I$  are preferred, the density of the mantle must be higher than the density of Mg-rich olivine and/or pyroxene minerals. This can be achieved by Fe-rich material mixed in the mantle or by the presence of solid FeS in the outer solid shell (Boukaré et al., 2019; Hauck et al., 2013; Smith et al., 2012). Solid FeS has a density of  $\sim 4.5$   $g\cdot cm^{-3}$  at the pressure range of Mercury's mantle (Urakawa et al., 2004). There are, however, geochemical arguments that limit the abundance of FeS in Mercury's outer solid shell. The bulk amount S of Mercury inferred from chondritic compositions that are considered feasible for Mercury does not accommodate a solid FeS layer more than 90 km thick (Namur et al., 2016). Additionally, the concentration of titanium of Mercury's surface measured by MESSENGER is indicative of a solid FeS layer of at most 13 km thick, if present at all (Cartier et al., 2020).

The full range of Si concentrations for Mercury's core in the interior structure models of this study is between 0 wt% and 25 wt%. Interior structure models with the large  $I$  (0.3593  $MR^2$ ), and correspondingly high mantle density (3.43–3.68  $g\cdot cm^{-3}$ ) and large core (2,025–2,080 km; Figure 6), make up the solution

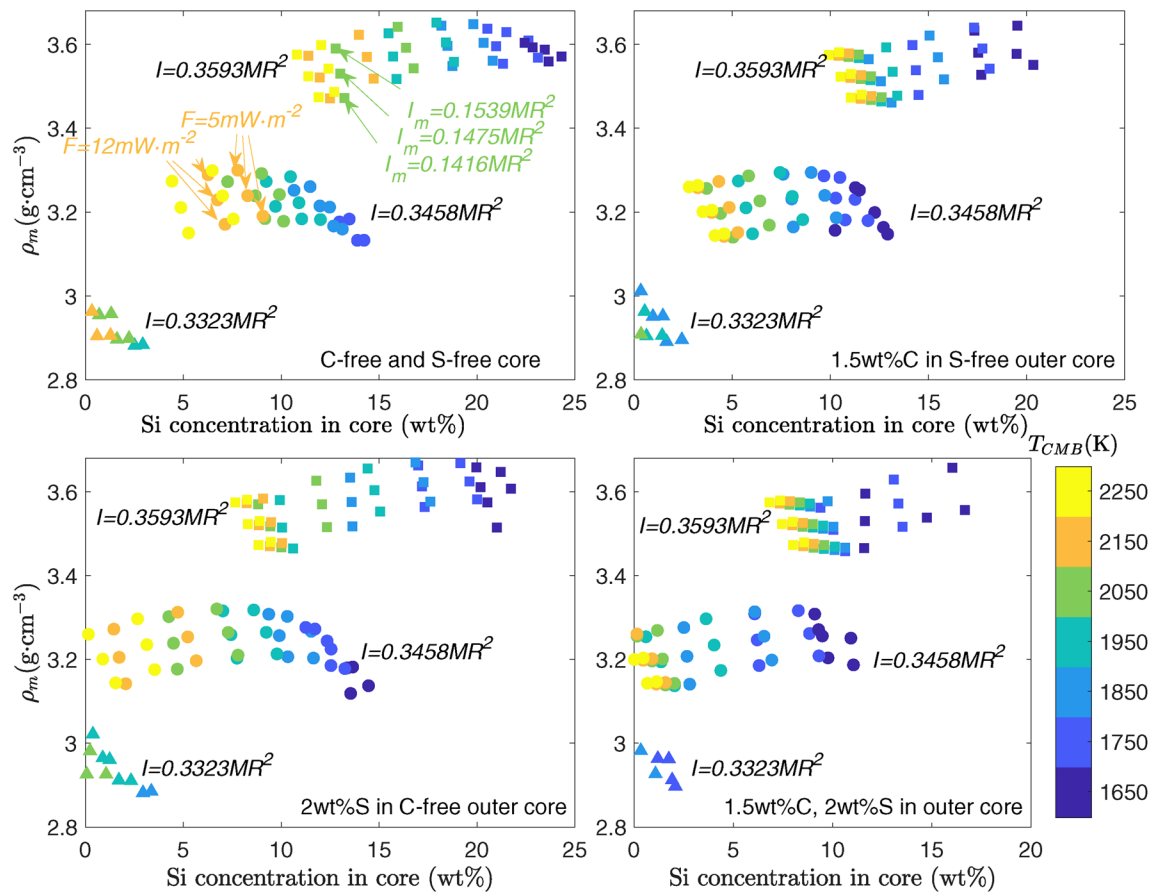


**Figure 7.** The density of the mantle (i.e., the density of the outer solid shell below the crust-mantle boundary assumed at 2,400 km radius) ( $\rho_m$ ) plotted against the Si-concentration of the core for interior structure models in the study. Interior structure models are C-free and S-free (upper left plot) or have additional 1.5 wt% C (upper right and lower left plot) and 2 wt% S (lower plots) in the core liquid. Symbols indicate the planetary moment of inertia of the interior structure models  $I = 0.3323 MR^2$  (triangles),  $I = 0.3458 MR^2$  (circles), and  $I = 0.3593 MR^2$  (squares). Interior structure models have moment of inertia of the outer solid shell  $I_m$  of 0.1416  $MR^2$ , 0.1475  $MR^2$ , and 0.1539  $MR^2$ . Interior structure models with the small  $I_m$  have consistently lower mantle density than those with the central or large  $I_m$ , as indicated by text and arrows in the upper left plot. Adopted CMB temperatures of between 1650 K and 2250 K (separated by 100 K intervals) are indicated by color. Interior structure models have core heat fluxes of 5  $mW \cdot m^{-2}$  and 12  $mW \cdot m^{-2}$ . Interior structure models with 12  $mW \cdot m^{-2}$  heat flux consistently have a slightly lower Si concentration in the core than the interior structure models with 5  $mW \cdot m^{-2}$  heat flux, as indicated by text and arrows in the upper left plot. Figure E4 of supporting information shows these characteristics for interior structure models with 3 wt% C or 4.5 wt% C with and without additional 2 wt% S in the liquid outer core. CMB, core-mantle boundary.

space with high concentrations of Si in the core (Figure 7). Interior structure models with the central value of  $I$  (0.3458  $MR^2$ ), and corresponding 3.15–3.35  $g \cdot cm^{-3}$  mantle densities and 1,973–2,025 km core radii (Figure 6), have intermediate concentrations of Si of up to 14 wt% in the core (Figure 7). Interior structure models with the small  $I$  (0.3323  $MR^2$ ), and corresponding low mantle density (2.88–3.03  $g \cdot cm^{-3}$ ) and smaller core (1,915–1,965 km; Figure 6), make up the solution space with low (<4 wt% Si) concentrations of Si in the core (Figure 7). These (maximum for given  $I$ ) Si concentrations in Mercury's core are obtained by interior structure models with C-free and S-free cores and with the lowest considered CMB temperature of 1650 K. The Si-concentration in the core is significantly lower for interior structure models that incorporate C and S as additional core constituents and for interior structure models with higher CMB temperature. The maximum Si core concentrations for C-free and S-free interior structure models with the large, central, and small  $I$  of 25 wt%, 14 wt%, and 3 wt%, respectively, are lowered to 17 wt%, 11 wt%, and 2 wt%, respectively, if 1.5 wt% C and 2 wt% S are incorporated in the liquid core (Figure 7). The specific relation between CMB temperature and the core's composition depends on whether the core is fully liquid for the considered temperature range such that an increase of core temperature only influences the density profile through thermal expansion, or whether temperature additionally affects the size of the core. For the interior

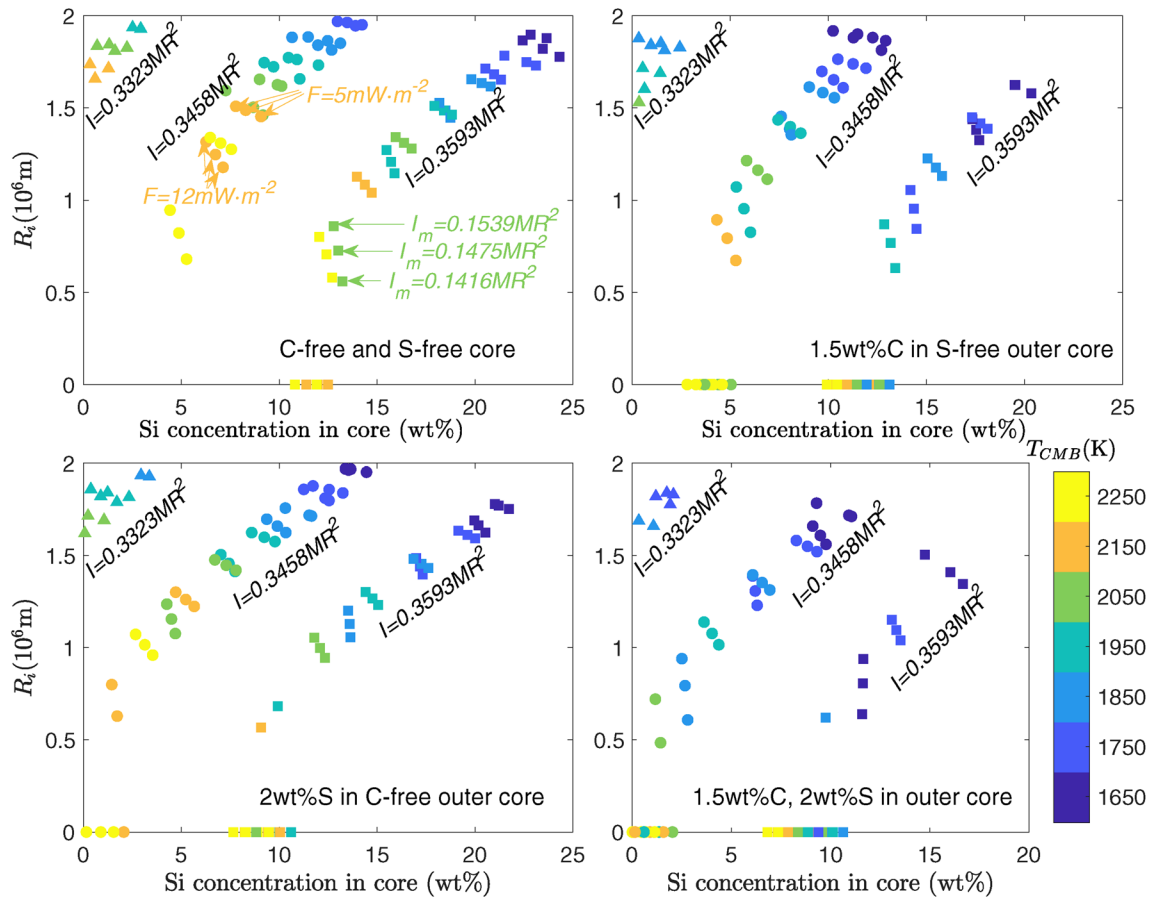


**Figure 8.** The radius of the inner core ( $R_i$ ) plotted against the Si-concentration of the core for interior structure models in the study. Interior structure models are C-free and S-free (upper left plot) or have additional 1.5 wt% C (upper right and lower left plot) and 2 wt% S (lower plots) in the core liquid. Symbols indicate the planetary moment of inertia of the interior structure models  $I = 0.3323 \text{ MR}^2$  (triangles),  $I = 0.3458 \text{ MR}^2$  (circles), and  $I = 0.3593 \text{ MR}^2$  (squares). The moment of inertia of the outer solid shell  $I_m$  for these interior structure models takes values of  $0.1416 \text{ MR}^2$ ,  $0.1475 \text{ MR}^2$ , or  $0.1539 \text{ MR}^2$ . Interior structure models with the small  $I_m$  have consistently slightly smaller inner core than those with the central or large  $I_m$ , as indicated by text and arrows in the upper left plot. Adopted CMB temperatures of between 1650 K and 2250 K (separated by 100 K intervals) are indicated by color. Interior structure models have core heat fluxes of  $5 \text{ mW}\cdot\text{m}^{-2}$  and  $12 \text{ mW}\cdot\text{m}^{-2}$ . Interior structure models with  $12 \text{ mW}\cdot\text{m}^{-2}$  heat flux consistently have a slightly lower Si concentration in the core and smaller inner core compared to the interior structure models with  $5 \text{ mW}\cdot\text{m}^{-2}$  heat flux, as indicated by text and arrows in the upper left plot. Figure E5 of supporting information shows these characteristics for interior structure models with 3 wt% C or 4.5 wt% C and with or without additional 2 wt% S in the liquid outer core. CMB, core-mantle boundary.

structure models plotted in Figure 7, models with CMB temperature of 2250 K have 8–14 wt% lower Si core concentrations compared to models with CMB temperature of 1650 K.

As discussed above, the size of the inner core is important for understanding Mercury's low-intensity magnetic field of broad-scale structure. Dynamo simulations with inner core radius smaller than  $\sim 1,200$  km and with a stably stratified liquid core layer on top of the dynamo region have produced low-intensity and broad-scale magnetic fields (Cao et al., 2014; Christensen, 2006; Christensen & Wicht, 2008; Manglik et al., 2010; Takahashi et al., 2019; Tian et al., 2015; Wardinski et al., 2020).

Only few interior structure models with binary Fe-Si core composition (C-free and S-free) of this study with the central or large  $I$  accommodate an inner core of  $<1,200$  km in radius (Figure 8, upper left panel). For interior structure models with the central  $I$ , an inner core of  $<1,200$  km in radius can only be met with a CMB temperature above  $\sim 2150$  K (Figure 8, upper left panel). These interior structure models have between 5 wt% Si and 8 wt% Si in the core. Thermal evolution studies of Mercury yield present-day CMB-temperatures of Mercury between  $\sim 1600$  K and  $\sim 2100$  K (Knibbe & van Westrenen, 2018; Michel et al., 2013; Tosi et al., 2013) and thus do not support CMB temperatures of  $>2150$  K. Additionally, such high CMB

temperatures are supersolidus with respect to lithologies that are expected in Mercury's lower mantle (e.g., Namur et al., 2016). Unless a thermal boundary layer is present at the CMB with a temperature discontinuity of several hundred degrees, CMB temperatures higher than 2150 K are expected to induce active volcanism from partial melting of the deep mantle. The geology of Mercury's surface suggests that widespread volcanism has ended at around 3.6 billion years ago (Byrne et al., 2016). For interior structure models with the large  $I$ , an inner core of <1,200 km in radius can be met with CMB temperature above 1950 K (Figure 8, upper left panel). These interior structure models have between 11 wt% Si and 15 wt% Si in the core and require a dense mantle of between  $3.43 \text{ g}\cdot\text{cm}^{-3}$  and  $3.68 \text{ g}\cdot\text{cm}^{-3}$ , as is discussed above. Thermal evolution scenarios have been presented with such CMB temperature of >1950 K (e.g., Knibbe & van Westrenen, 2018), but the dense FeS that may be needed in the outer solid shell to obtain such a high mantle density has a melting temperature of between 1500 K and 1700 K at the pressure of Mercury's deep mantle (Urakawa et al., 2004). Hence, a layer of FeS at the bottom of the outer solid shell (e.g., Smith et al., 2012) would be in liquid phase if CMB temperatures are higher than  $\sim 1700 \text{ K}$  (e.g., Michel et al., 2013) and would not take part of the librations of the outer solid shell. If FeS is present in the outer solid shell as an explanation for a high mantle density with such high CMB temperatures, the FeS must reside in the upper colder part of the mantle. This requires resistivity against gravitational sorting of the dense FeS ( $\sim 4.5 \text{ g}\cdot\text{cm}^{-3}$ ) and the silicates ( $3.11\text{--}3.26 \text{ g}\cdot\text{cm}^{-3}$ ) throughout the entire evolution of Mercury's mantle. To summarize, for a core of binary Fe-Si alloy, it is difficult to obtain a small radius (<1,200 km) of the inner core that is consistent with dynamo simulations for Mercury's magnetic field (Figure 8, upper left panel).

Interior structure models with 1.5 wt% C and 2 wt% S in the core and with the central value for  $I$  are calculated with inner cores smaller than 1,200 km in radius with CMB temperatures as low as 1850 K (Figure 8, lower right panel). Fully liquid cores have been obtained for these models with CMB temperatures as low as 1950 K. Such CMB temperatures are in the warm range of present-day CMB temperatures obtained by thermal evolution studies for Mercury (1600–2100 K) (Knibbe & van Westrenen, 2018; Michel et al., 2013; Tosi et al., 2013). These interior structure models have mantle densities that are consistent with Mg-rich minerals that are inferred for the mantle of Mercury, as discussed above. These interior structure models with <1,200 km inner core radius have Si contents of the core lower than  $\sim 7 \text{ wt}\%$ . Interior structure models with ternary (Fe-Si-C) or quaternary cores (Fe-Si-C-S) with the large  $I$  and <1,200 km inner core radius have up to 16 wt% Si in the core (for example the S-free interior structure models with 1.5 wt% C in the liquid core of Figure 8). CMB temperatures of these interior structure models span the entire range of CMB temperatures that are obtained by thermal evolution studies (Figure 8). Although these interior structure models have a denser outer solid shell compared to the density of Mg-rich minerals inferred for the mantle of Mercury, as discussed above, such interior structure models with relatively cold CMB temperatures may allow for a solid FeS layer to be present at the bottom of the solid outer shell.

Interior structure models with the small  $I$  have an inner core radius larger than  $\sim 1,600 \text{ km}$  (Figure 8).

#### 4.2. Consequences of Core-mantle Coupling on Mercury's Interior Structure

The influence of core-mantle coupling on the obliquity  $\theta$  and on the amplitude of physical librations  $\psi$  of Mercury's surface is examined in text E of supporting information. A gravitational torque exerted by an ellipsoidal inner core on the outer solid shell may increase  $\theta$  compared to the value calculated for a rigid planet by Peale's equation (Equation E13 of text E of supporting information; Peale et al., 2016). The magnitude of this influence on the interior structure models of this study is not well known (Text E of supporting information). Peale et al. (2016) performed spin-evolution simulations on simplified interior structure models of Mercury to study this effect. For interior structure models that most closely resemble the interior structure models in this study, their spin-evolution simulations suggest that this coupling may increase  $\theta$  by more than the  $\pm 0.08 \text{ arcmin}$  uncertainty margin of Margot et al. (2012), if the inner core radius is larger than  $\sim 1,200 \text{ km}$  (Figure E5 of supporting information). Such influence is much larger than the effect of an inner core on the obliquity of Mercury's surface that is calculated by Baland et al. (2017) of about 1% ( $0.02 \text{ arcmin}$ ) or less. If the larger influence by inner core coupling derived by Peale et al. (2016) would be accounted for, the interior structure models with the large  $I$  ( $0.3593 \text{ MR}^2$ ) and a significant inner core would correspond to a surface obliquity that is larger than the  $2.04 \pm 0.08 \text{ arcmin}$  measured by Margot

et al. (2012). Additionally, interior structure models with an inner core radius larger than  $\sim 1,200$  km and  $I$  smaller than the smallest value used in this study ( $0.3323 \text{ MR}^2$ ) could be consistent with a surface obliquity in the measured range of  $2.04 \pm 0.08$  arcmin. Interior structure models with the small  $I$  presented in this study accommodate low amounts of light elements in the core ( $<4 \text{ wt\% Si}$ ), have a larger inner core ( $>\sim 1,600$  km in radius; Figure 7), and a low mantle density ( $2.88\text{--}3.03 \text{ g}\cdot\text{cm}^{-3}$ ; Figure 6). Interior structure models with smaller  $I$  than examined in this study would require an even larger inner core, a higher density than pure Fe for the core that is completely devoid of light core alloying elements, and require a further lowered mantle density. Hence, interior structure models that could be consistent with the measured obliquity of Mercury as a result of inner core coupling, but which are not spanned by the interior structure models of this study, are problematic in light of the present-day understanding of the planet.

Core-mantle coupling tends to decrease the amplitude of forced librations in longitude  $\psi$  for interior structure models with an inner core, compared to the value calculated by Peale's equation (Equation E14 of text E in supporting information; Van Hoolst et al., 2012; Dumberry et al., 2013). We use the same approach as in Rivoldini and Van Hoolst (2013) to estimate the influence for core-mantle coupling on  $\psi$  (Text E in supporting information). For interior structure models with the inner core radius smaller than 1,400 km, we obtained values of  $\psi$  for interior structure models of this study that are up to 1% ( $\sim 0.4$  arcsec) lower than calculated by Peale's equation (Figure E7 of supporting information). For interior structure models with the inner core radius between 1,700 km and 1,800 km, we obtain values of  $\psi$  for the interior structure models of this study that are up to 4.1% ( $\sim 1.6$  arcsec) lower than calculated by Peale's equation (i.e., the  $\pm$  uncertainty as observed by Margot et al., 2012). This implies that the interior structure models of this study with the large  $I_m$  ( $0.1539 \text{ MR}^2$ ) and an inner core radius larger than  $\sim 1,700$  km may correspond to a libration amplitude of Mercury's surface that is by about 1.6 arcsec smaller than the reported lower observational limit for  $\psi$  of 35.9 arcsec of Mercury (Margot et al., 2012). This also implies that, interior structure models with an  $I_m$  significantly smaller than the smallest value explored in this study ( $0.1416 \text{ MR}^2$ ) and inner core larger than  $\sim 1,700$  km in radius could be consistent with the  $\psi$  of  $38.5 \pm 1.6$  arcsec observed for Mercury (Margot et al., 2012).

## 5. Implications

### 5.1. Implications for the Bulk Composition of Mercury

The primitive (CB) bencubbinite chondrites (e.g., Weisberg et al., 2001) and EH enstatite chondrite (Cartier et al., 2014; McCoy et al., 1999) are strongly reduced. These chondrites are in various studies mentioned as compositional analogs for Mercury (e.g., Taylor & Scott, 2003). Although the origin of the CB chondrites is still under debate (Petaev et al., 2001; Weisberg et al., 2001; Weyrauch et al., 2019; and references therein) the CB chondrites have a metal to silicate ratio that is similar to that of Mercury. Accretion of this or a similar chondrite type may explain the large Fe fraction of Mercury (Taylor & Scott, 2003). The EH chondrites have a much larger silicate fraction (70–80 wt%) than that of Mercury. An analogy between the EH and Mercury requires the removal of silicates from Mercury or an enrichment of metallic Fe for Mercury to account for the planet's large Fe fraction of between 60 wt% and 80 wt%.

The detection of C on Mercury's surface has been interpreted as an indication that Mercury's metallic core could be saturated in C (e.g., Steenstra & van Westrenen, 2020; Vander Kaaden et al., 2020). This view has recently led to new estimates for the core composition of Mercury from assumed chondritic, including an EH chondrite-like or CB chondrite-like, bulk compositions of the planet (Steenstra & van Westrenen, 2020; Vander Kaaden et al., 2020). The Si and C core concentrations of an EH chondrite-like bulk composition of Mercury are estimated at  $18.9 \pm 1.8 \text{ wt\% Si}$  and  $0.36 \pm 0.19 \text{ wt\% C}$  by Steenstra and van Westrenen (2020), whereas Vander Kaaden et al. (2020) obtained Si and C core concentrations of 27 wt% Si and between 0.4 wt% C and 0.5 wt% C. Assuming a CB chondrite-like bulk composition of Mercury, Si and C core concentrations are estimated at between 4.5 wt% Si and 14.3 wt% Si and between 0.5 wt% C and 4.3 wt% C by Steenstra and van Westrenen (2020). The specific obtained core composition depends on the specific chondrite type ( $\text{Cb}_a$  or  $\text{Cb}_b$ ) and whether the chondrite is C-saturated. Vander Kaaden et al. (2020) obtained between 5 wt% Si and 18.5 wt% Si and between 0.8 wt% C and 4.0 wt% C in Mercury's core, from an assumed CB



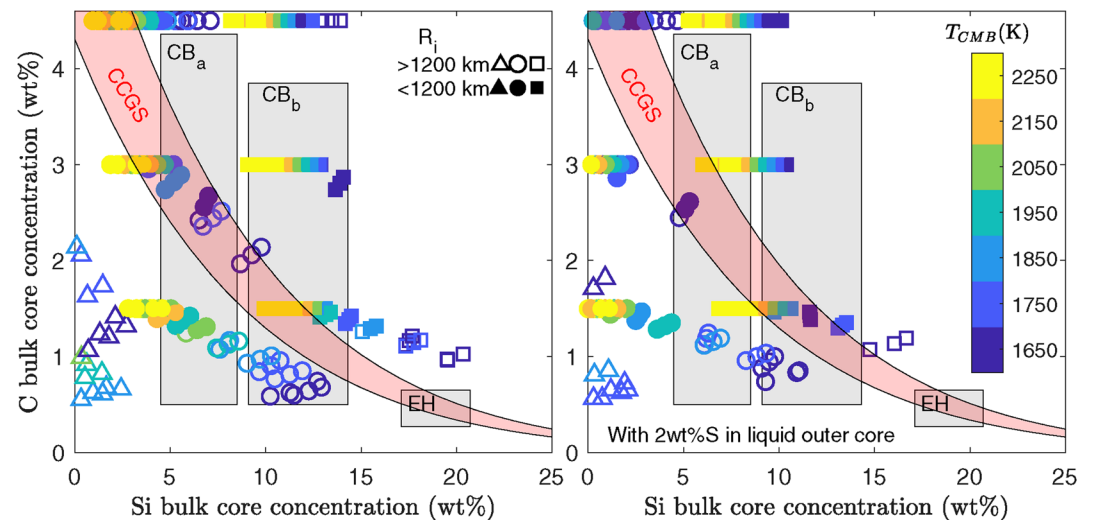


**Figure 9.** The composition of the bulk core of the interior structure models of this study. Symbols indicate the planetary moment of inertia of the interior structure models  $I = 0.3323 \text{ MR}^2$  (triangle),  $I = 0.3458 \text{ MR}^2$  (circles), and  $I = 0.3593 \text{ MR}^2$  (squares). The left plot shows interior structure models with S-free core composition. The right plot shows interior structure models with 2 wt% S in the liquid outer core. Open symbols are used for interior structure models with a radius of the inner core larger than 1,200 km. Filled symbols are used for interiors structure models with an inner core radius smaller than 1,200 km. Translucent gray-scaled areas indicate the bulk core composition of Mercury from a CB<sub>a</sub>, CB<sub>b</sub>, or EH chondrite bulk composition of Mercury as estimated by Steenstra and van Westrenen (2020). The translucent red-scales area indicates the carbon concentration at graphite saturation (CCGS) estimated at 5 GPa and between 1700 K and 2200 K using the parametrization for CCGS of Steenstra et al. (2020). The influence of S is not incorporated in the parametrization for CCGS. Adopted CMB temperatures of between 1650 K and 2250 K (separated by 100 K intervals) are indicated by color. CMB, core-mantle boundary.

chondrite-like bulk composition for Mercury. These studies are not in exact agreement about the estimated composition of Jurrien Sebastiaan Knibbe

Mercury's core, particularly when an EH chondrite-like bulk composition is assumed for Mercury. Nonetheless, the estimated Si concentration of Mercury's core is consistently lower for an assumed CB chondrite-like bulk composition of Mercury compared to that estimated from an assumed EH chondrite-like bulk composition of Mercury.

The estimated core composition for an EH chondrite-like Mercury by Vander Kaaden et al. (2020) cannot be met by any interior structure model of this study. Only the interior structure models in this study with the large  $I$  ( $0.3593 \text{ MR}^2$ ) and high mantle densities ( $3.43\text{--}3.68 \text{ g}\cdot\text{cm}^{-3}$ ) accommodate a Si content of Mercury's core higher than 14 wt% Si (Figure 9). Only the colder ( $<1850 \text{ K}$  CMB temperature) of those interior structure models, for which the inner core is larger than 1,200 km, have a core composition near that estimated for an EH chondrite-like Mercury by Steenstra and van Westrenen (2020) (Figure 9). The relatively dense mantle and significant inner core size ( $>1,200 \text{ km}$  in radius) of these interior structure models have direct implications for the mantle geochemistry and for the generation of Mercury's magnetic field, which is thought to be generated by a deep liquid dynamo layer (Cao et al., 2014; Christensen, 2006; Christensen & Wicht, 2008; Manglik et al., 2010; Takahashi et al., 2019; Tian et al., 2015; Wardinski et al., 2020).

The Si and C concentrations of Mercury's core that are estimated from assuming a CB-like bulk composition of Mercury are met by interior structure models of this study with the central  $I$  ( $0.3458 \text{ MR}^2$ ; Figure 9, left). These interior structure models have mantle densities of between  $3.15 \text{ g}\cdot\text{cm}^{-3}$  and  $3.35 \text{ g}\cdot\text{cm}^{-3}$  and a S-free core composition in the range of Fe-(0–14 wt%) Si-(1–5 wt%) C. The C-concentration of the core strongly decreases with increasing Si concentrations of the core (Figure 9). Among these interior structure models, the interior structure models with a Si-poor core ( $<\sim 7.5 \text{ wt}\%$  Si) have an inner core smaller than 1,200 km, whereas the Si-rich ( $>\sim 7.5 \text{ wt}\%$  Si) interior structure models have a larger inner core. The core

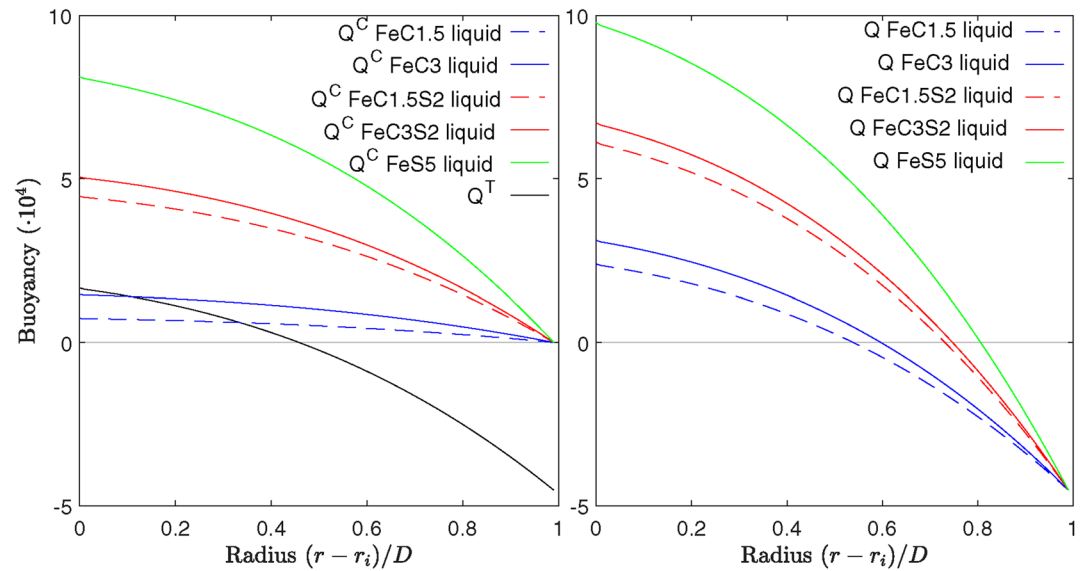


**Figure 10.** Calculated buoyancy profiles of the liquid core. (left) Profiles of compositional buoyancy  $Q^C$  and thermal buoyancy  $Q^T$  (black solid) of liquid cores with 1.5 wt% C (blue dashed), 3 wt% C (blue solid), 1.5 wt% C and 2 wt% S (red dashed), 3 wt% C and 2 wt% S (red solid), and 5 wt% S (green). (right) Profiles of co-density buoyancy  $Q = Q^C + Q^T$  of the liquid core, of which  $Q^C$  and  $Q^T$  are shown in the left plot. Buoyancy profiles are calculated by the procedure of Christensen and Wicht (2008) (see Text G in supporting information). An inner core radius of 800 km is used in these calculations.

concentration of Si is lowered by about 3 wt% for interior structure models where 2 wt% S is added to the liquid outer core (Figure 9, compare left panel with right panel).

The interior structure models with the small  $I$  ( $0.3323 \text{ MR}^3$ ) have less than 4 wt% Si and less than 2.5 wt% C in Mercury's core (Figure 9). These core compositions are outside the range of core compositions that are estimated by assuming EH chondrite-like and CB chondrite-like bulk compositions of the planet.

## 5.2. Implications for Mercury's Core Dynamo

A certain amount of S and/or C in the liquid core of Mercury appears to be necessary to obtain a small size of the inner core that is in line with published dynamo simulations for Mercury (Section 4). Both S and C (at the Fe-rich side of the Fe-Fe<sub>3</sub>C eutectic with corresponding C concentration of below  $\sim 3\text{--}4$  wt% C) partition preferentially into the core liquid. This partitioning behavior gives rise to compositional buoyancy upon inner core solidification which, in addition to thermal buoyancy, reigns the dynamics in the outer core of Mercury.

Figure 10 shows thermal and compositional buoyancy profiles of liquid cores with Fe-1.5 wt% C, Fe-3 wt% C, Fe-1.5 wt% C-2 wt% S, Fe-3 wt% C-2 wt% S, and Fe-5 wt% S composition, computed by the procedure of Christensen and Wicht (2008; Text G in supporting information). Because S partitions exclusively in the liquid outer core and strongly decreases the density of Fe-rich liquid metal (Figure 5), the partitioning of S upon core solidification leads to a strong compositional buoyancy. Adding only 2 wt% S to the liquid core of Mercury gives rise to a compositional buoyancy at the inner core boundary that is more than two times the thermal buoyancy. In a liquid core of binary Fe-(1.5 or 3) wt% C, the compositional buoyancy is much weaker and of magnitude similar to that of thermal buoyancy (Figure 10). The compositional buoyancy is reduced in the upper region of the core compared to the lower region of the liquid core. This results from an assumed uniform compositional sink in the liquid outer core and neglecting compositional interaction with the mantle (Text G in supporting information). The thermal buoyancy profiles calculated here are strongly negative in the upper region of the core as a result of the subadiabatic heat flux at the CMB. Combined, the sum of compositional and thermal buoyancy (co-density) is negative (stabilizing) in the uppermost region

of the liquid core. The negatively buoyant (stably stratified) region is smaller in scenarios with S in the liquid core compared to if S is absent (Figure 10).

The co-density buoyancy approximation, that is, that the effective buoyancy is equal to the sum of compositional and thermal buoyancy, neglects that compositional diffusivity is several orders of magnitude higher than thermal diffusivity (e.g., Manglik et al., 2010, and references therein). Manglik et al. (2010) showed double diffusive dynamo simulations with a strong compositional buoyancy component that have convective flows in the uppermost layer that lead to a stronger magnetic field of Mercury than is observed by spacecraft, even if this region would be stratified in the co-density approximation. Takahashi et al. (2019), however, published double diffusive dynamo simulations with thermal and compositional buoyancy, of which some simulations yielded a long-lived magnetic field that is consistent with the measurements of Mercury's magnetic field (e.g., the BU1 simulation of Takahashi et al., 2019). It is perhaps testable whether diffusive dynamo simulations with a large (representative for S-containing liquid cores) or a small (representative for Fe-Si-C liquid cores) ratio of compositional to thermal buoyancy are preferential for obtaining a magnetic field of Mercury.

Interior structure models with more than 4 wt% C have a core composition at the C-rich side of the Fe-Fe<sub>3</sub>C eutectic. For such core alloy, C is not expected to fractionate preferentially in the liquid outer core. This would reduce (or perhaps completely remove) the compositional buoyancy in a ternary Fe-Si-(>4 wt%) C liquid core. Furthermore, Fe-snow scenarios with consequent strong compositional stratification in Mercury's outer core have been proposed for binary Fe-S core alloy of Mercury. This may occur if the S concentration in Mercury's liquid outer core is larger than ~5 wt% (Dumberry & Rivoldini, 2015; Chen et al., 2008; Vilim et al., 2010). These scenarios are not examined here because such S-rich core composition are not in line with the inferred reduced nature of the planet (Chabot et al., 2014; Namur et al., 2016; Steenstra & van Westrenen, 2020; Vander Kaaden et al., 2020).

## 6. Summary

This study presents measurements of density by X-ray absorption techniques and of P-wave velocity ( $V_P$ ) by ultrasonic techniques of liquid Fe-(<17 wt%) Si-(<4.5 wt%) C alloys at pressures up to 5.8 GPa. The measured density decreases more strongly with increasing Si-concentration than suggested by measurements of Tateyama et al. (2011) and Sanloup et al. (2004). The density and  $V_P$  measurements reported in this study are relatively consistent with the measurements of Terasaki et al. (2019) and Yu and Secco (2008). The measured  $V_P$  increases with Si concentration, which is consistent with Williams et al. (2015) and Terasaki et al. (2019). The measured  $V_P$  on near-binary Fe-17 wt% Si is, however, not sufficiently high to support the (low) densities of liquid Fe-15 wt% Si-5 wt% Ni measured at high pressures of 30–100 GPa by Morard et al. (2013). The experimental data are modeled by a ternary liquid Fe-Si-C ideal mixing model (FESIC). This model is consistent with literature data at ambient conditions and with literature high-pressure density and  $V_P$  data of binary liquid Fe-C.

The FESIC mixing model characterizes the liquid core in new interior structure models of planet Mercury. The interior structure models are constrained by the planet's moment of inertia ( $I$ ) and that of the outer solid shell ( $I_m$ ), which are calculated from the measurements of Mercury's obliquity ( $\theta$ ) and forced librations in longitude ( $\psi$ ) (Margot et al., 2012). Small, central and large values of  $I$  and  $I_m$  are used, which correspond to the  $\pm$  uncertainty margins of the measured  $\theta$  and  $\psi$  by Margot et al. (2012). The computed interior structure models are most in line with the density of the mantle that is inferred from geochemical inferences of Mercury's surface if the central value for  $I$  is adopted. These interior structure models can only accommodate an inner core of less than 1,200 km in radius, in agreement with published dynamo simulations studies on Mercury (e.g., Christensen, 2006; Christensen & Wicht, 2008; Takahashi et al., 2019), if S and/or C are present in Mercury's liquid core at the wt% level.

Interior structure models with the central value of  $I$  have a Si concentration of the core of below ~14 wt% for binary Fe-Si core alloy. The concentration of Si in Mercury's core is significantly reduced if additional C or S is present in the core and if the inner core is small. The obtained abundances of light elements in Mercury's core are lower than that is estimated from metal-silicate fractionation of an EH chondrite by

Steenstra and van Westrenen (2020) and Vander Kaaden et al. (2020). A core composition of Mercury with lower concentrations in light elements, as inferred from assuming a bulk planet composition that is based on the CB chondrite, can be met by bulk core composition interior structure models that are calculated with the central value of  $I$ .

The presence of C and/or S in Mercury's liquid core likely goes paired with compositional buoyancy in the liquid core. The compositional buoyancy in an Fe-Si-C liquid core is similar in magnitude to that expected for thermal buoyancy. The compositional buoyancy is likely significantly larger than thermal buoyancy if S is also present in the liquid outer core of Mercury. These relations can be relevant for the understanding of dynamo generation in the liquid core of Mercury.

## Data Availability Statement

Raw experimental data, the matlab code used for data-analysis, and the interior structure models of Mercury are published in the Zenodo online repository (Knibbe, 2020).

## Acknowledgments

We thank the editor Laurent Montesi for the handling of the manuscript submission process. We also thank the associate editor and two anonymous reviewers for providing constructive comments that have helped to improve the study. The X-ray absorption measurements were performed on beamline ID-27 at the European Synchrotron Radiation Facility (ESRF), Grenoble, France. The ultrasonic measurements of this study were performed at HPCAT (Sector 16), Advanced Photon Source (APS), Argonne National Laboratory. The Advanced Photon Source is a U.S. Department of Energy (DOE) Office of Science User Facility operated for the DOE Office of Science by Argonne National Laboratory under Contract No. DE-AC02-06CH11357. HPCAT is supported by DOE-NNSA's Office of Experimental Sciences. This project has received funding from the European Union's Horizon 2020 research and innovation program under the Marie Skłodowska-Curie grant agreement MERCURYREFINEMENT, with No 845354, awarded to JSK. Throughout the course of this project, JSK also received funding by the KU Leuven (PDM contract) and a postdoctoral Marie-Curie Seal of Excellence fellowship (12Z622ON) of the FWO-Flanders. Initial data were obtained with financial support from a Netherlands Space Office User Support Program grant to WvW and a BRAIN-be program grant (BR/143/A2/COME-IN) to TVH. BC is a Research Associate of the Belgian Fund for Scientific Research-FNRS.

## References

- Anderson, B. J., Johnson, C. L., Korth, H., Winslow, R. M., Borovsky, J. E., Purucker, M. E., et al. (2012). Low-degree structure in Mercury's planetary magnetic field. *Journal of Geophysical Research*, 117, E00L12. <https://doi.org/10.1029/2012JE004159>
- Anzellini, S., Dewaele, A., Mezouar, M., Loubeyre, P., & Morard, G. (2013). Melting of iron at Earth's inner core boundary based on fast X-ray diffraction. *Science*, 340(6131), 464–466. <https://doi.org/10.1126/science.1233514>
- Asphaug, E., & Reufer, A. (2014). Mercury and other iron-rich planetary bodies as relics of inefficient accretion. *Nature Geoscience*, 7, 564–568. <https://doi.org/10.1038/ngeo2189>
- Baland, R.-M., Yseboodt, M., Van Hoolst, T., & Rivoldini, A. (2017). The influence of the fluid outer core and of the solid inner core on the orientation of the rotation axis of Mercury. *EPSC Abstracts*, 11, EPSC20175211.
- Benz, W., Slattery, W. L., & Cameron, A. G. W. (1988). Collisional stripping of Mercury's mantle. *Icarus*, 74(3), 516–528. [https://doi.org/10.1016/0019-1035\(88\)90118-2](https://doi.org/10.1016/0019-1035(88)90118-2)
- Berthet, S., Malavergne, V., & Righter, K. (2009). Melting of the Indarch meteorite (EH4 chondrite) at 1 GPa and variable oxygen fugacity: Implications for early planetary differentiation processes. *Geochimica et Cosmochimica Acta*, 73(20), 6402–6420. <https://doi.org/10.1016/j.gca.2009.07.030>
- Beuthe, M., Charlier, B., Namur, O., Rivoldini, A., & Van Hoolst, T. (2020). Mercury's crustal thickness correlates with lateral variations in mantle melt production. *Geophysical Research Letters*, 47(9). <https://doi.org/10.1029/2020GL087261>
- Boujibar, A., Andrault, D., Bouhifd, M. A., Bolfan-Casanova, N., Devidal, J.-L., & Trcera, N. (2014). Metal-silicate partitioning of Sulphur, new experimental and thermodynamic constraints on planetary accretion. *Earth and Planetary Science Letters*, 391, 42–54. <https://doi.org/10.1016/j.epsl.2014.01.021>
- Boukaré, C.-E., Parman, S. W., Parmentier, E. M., & Anzures, B. A. (2019). Production and preservation of sulfide layering in Mercury's mantle. *Journal of Geophysical Research: Planets*, 124(12), 3354–3372. <https://doi.org/10.1029/2019JE005942>
- Byrne, P. K., Ostrach, L. R., Fasset, C. I., Chapman, C. R., Denevi, B. W., Evans, A. J., et al. (2016). Widespread effusive volcanism on Mercury likely ended by about 3.5 GPa. *Geophysical Research Letters*, 43(14), 7408–7416. <https://doi.org/10.1002/2016GL069412>
- Cameron, A. G. W. (1985). The partial volatilization of Mercury. *Icarus*, 64(2), 285–294. [https://doi.org/10.1016/0019-1035\(85\)90091-0](https://doi.org/10.1016/0019-1035(85)90091-0)
- Cao, H., Aurnou, J. M., Wicht, J., Dietrich, W., Soderlund, K. M., & Russell, C. T. (2014). A dynamo explanation for Mercury's anomalous magnetic field. *Geophysical Research Letters*, 41(12), 4127–4134. <https://doi.org/10.1002/2014GL060196>
- Cartier, C., Hammouda, T., Doucelance, R., Boyet, M., Devidal, J.-L., & Moine, B. (2014). Experimental study of trace element partitioning between enstatite and melt in enstatite chondrites at low oxygen fugacities and 5 GPa. *Geochimica et Cosmochimica Acta*, 130, 167–187. <https://doi.org/10.1016/j.gca.2014.01.002>
- Cartier, C., Namur, O., Nittler, L. R., Weider, S. Z., Crapster-Pregont, E., Vorburger, A., et al. (2020). No FeS layer in Mercury? Evidence from Ti/Al measured by MESSENGER. *Earth and Planetary Science Letters*, 534, 116108. <https://doi.org/10.1016/j.epsl.2020.116108>
- Chabot, N. L., Wollack, E. A., Klima, R. L., & Minitti, M. E. (2014). Experimental constraints on Mercury's core composition. *Earth and Planetary Science Letters*, 390, 199–208. <https://doi.org/10.1016/j.epsl.2014.01.004>
- Charlier, B., & Namur, O. (2019). The origin and differentiation of planet Mercury. *Elements*, 15(1), 9–14. <https://doi.org/10.2138/gselements.15.1.9>
- Chau, A., Reinhardt, C., Helled, R., & Stadel, J. (2018). Forming Mercury by giant impacts. *The Astrophysical Journal*, 865(1), 35. <https://doi.org/10.3847/1538-4357/aad8b0>
- Chen, B., Li, J., & Hauck, S. A. (2008). Non-ideal liquidus curve in the Fe-S system and Mercury's snowing core. *Geophysical Research Letters*, 35(7). <https://doi.org/10.1029/2008GL033311>
- Christensen, U. R. (2006). A deep dynamo generating Mercury's magnetic field. *Nature*, 444, 1056–1058. <https://doi.org/10.1038/nature05342>
- Christensen, U. R., & Wicht, J. (2008). Models of magnetic field generation in partly stable planetary cores: Applications to Mercury and Saturn. *Icarus*, 196(1), 16–34. <https://doi.org/10.1016/j.icarus.2008.02.013>
- Dasgupta, R., Walker, D. (2008). Carbon solubility in core melts in a shallow magma ocean environment and distribution of carbon between the Earth's core and the mantle. *Geochimica et Cosmochimica Acta*, 72, (18), 4627–4641. <https://doi.org/10.1016/j.gca.2008.06.023>
- Dorogokupets, P. I., Dymshits, A. M., Litasov, K. D., & Sokolova, T. S. (2017). Thermodynamics and equations of state of iron to 350 GPa and 6000 K. *Scientific Reports*, 7(1), 1–10. <https://doi.org/10.1038/srep41863>



- Dubrovinsky, L. S., Saxena, S. K., & Lazor, P. (1998). High-pressure and high-temperature in situ X-ray diffraction study of iron and corundum to 68 GPa using an internally heated diamond anvil cell. *Physics and Chemistry of Minerals*, 25, 434–441. <https://doi.org/10.1007/s002690050133>
- Dumberry, M., & Rivoldini, A. (2015). Mercury's inner core size and core-crystallization regime. *Icarus*, 248, 254–268. <https://doi.org/10.1016/j.icarus.2014.10.038>
- Dumberry, M., Rivoldini, A., Van Hoolst, T., & Yseboodt, M. (2013). The role of Mercury's core density structure on its longitudinal librations. *Icarus*, 225(1), 62–74. <https://doi.org/10.1016/j.icarus.2013.03.001>
- Ebel, D. S., & Stewart, S. T. (2018). The elusive origin of Mercury. In S. C. Solomon, L. R. Nittler, & B. J. Anderson (Eds.), *Mercury: The view after MESSENGER* (Ch 18, pp. 497–515). Cambridge, UK: Cambridge University Press.
- Fegley, B., Jr., & Cameron, A. G. W. (1987). A vaporization model for iron/silicate fractionation in the Mercury protoplanet. *Earth and Planetary Science Letters*, 82(3–4), 207–222. [https://doi.org/10.1016/0012-821X\(87\)90196-8](https://doi.org/10.1016/0012-821X(87)90196-8)
- Fei, Y., Bertka, C. M., & Finger, L. W. (1997). High-pressure iron-sulfur compound, Fe<sub>3</sub>S<sub>2</sub>, and melting relations in the Fe-FeS system. *Science*, 275(5306), 1621–1623. <https://doi.org/10.1126/science.275.5306.1621>
- Fei, Y., & Brosh, E. (2014). Experimental study and thermodynamical calculations of phase relations in the Fe-C system at high pressure. *Earth and Planetary Science Letters*, 408, 155–162. <https://doi.org/10.1016/j.epsl.2014.09.044>
- Fei, Y., Ricolleau, A., Frank, M., Mibe, K., Shen, G., & Prakapenka, V. (2007). Toward an internally consistent pressure scale. *Proceedings of the National Academy of Sciences of the United States of America*, 104(22), 9182–9186. <https://doi.org/10.1073/pnas.0609013104>
- Fischer, R. A., Campbell, A. J., Caracas, R., Reaman, D. M., Dera, P., & Prakapenka, V. B. (2012). Equation of state and phase diagram of Fe-16Si alloy as a candidate component of Earth's core. *Earth and Planetary Science Letters*, 357–358, 268–276. <https://doi.org/10.1016/j.epsl.2012.09.022>
- Fischer, R. A., Campbell, A. J., Caracas, R., Reaman, D. M., Heinz, D. L., Dera, P., & Prakapenka, V. B. (2013). Equations of state in the Fe-FeSi system at high pressures and temperatures. *Journal of Geophysical Research: Solid Earth*, 119(4), 2810–2827. <https://doi.org/10.1002/2013JB010898>
- Genova, A., Goossens, S., Mazarico, E., Lemoine, F. G., Neumann, G. A., Kuang, W., et al. (2019). Geodetic evidence that Mercury has a solid inner core. *Geophysical Research Letters*, 46(7), 3625–3633. <https://doi.org/10.1029/2018GL081135>
- Hauck, S. A., Margot, J. L., Solomon, S. C., Phillips, R. J., Johnson, C. J., Lemoine, F. G., et al. (2013). The curious case of Mercury's internal structure. *Journal of Geophysical Research: Planets*, 118(6), 1204–1220. <https://doi.org/10.1002/jgre.20091>
- Hubbard, A. (2014). Explaining Mercury's density through magnetic erosion. *Icarus*, 241, 329–335. <https://doi.org/10.1016/j.icarus.2014.06.032>
- Jimbo, I., & Cramb, A. W. (1993). The density of liquid iron-carbon alloys. *Metallurgical Transactions B*, 24, 5–10. <https://doi.org/10.1007/BF02657866>
- Kawai, Y., Mori, K., Kishimoto, M., Ishikura, K., & Shimada, T. (1974). Surface tension of liquid Fe-C-Si alloys. *Tetsu-to-Hagane*, 60(1), 29–37. [https://doi.org/10.2355/tetsutohagane1955.60.1\\_29](https://doi.org/10.2355/tetsutohagane1955.60.1_29)
- Kilburn, M. R., & Wood, B. J. (1997). Metal-silicate partitioning and the incompatibility of S and Si during core formation. *Earth and Planetary Science Letters*, 152(1–4), 139–148. [https://doi.org/10.1016/S0012-821X\(97\)00125-8](https://doi.org/10.1016/S0012-821X(97)00125-8)
- Knibbe, J. S. (2020). Mercury's interior structure constrained by density and P-wave velocity measurements of liquid Fe-Si-C alloys[Data set]. <https://doi.org/10.5281/ZENODO.4090496>
- Knibbe, J. S., & van Westrenen, W. (2015). The interior configuration of planet Mercury constrained by moment of inertia and planetary contraction. *Journal of Geophysical Research: Planets*, 120(11), 1904–1923. <https://doi.org/10.1002/2015JE004908>
- Knibbe, J. S., & van Westrenen, W. (2018). The thermal evolution of Mercury's Fe-Si core. *Earth and Planetary Science Letters*, 482, 147–159. <https://doi.org/10.1016/j.epsl.2017.11.006>
- Komabayashi, T. (2014). Thermodynamics of melting relations in the system Fe-FeO at high pressure: Implications for oxygen in the Earth's core. *Journal of Geophysical Research: Solid Earth*, 119(5), 4164–4177. <https://doi.org/10.1002/2014JB010980>
- Kono, Y., Park, C., Sakamaki, T., Kenny-Benson, C., Shen, G., & Wang, Y. (2012). Simultaneous structure and elastic wave velocity measurement of SiO<sub>2</sub> glass at high pressure and high temperatures in a Paris-Edinburgh cell. *Review of Scientific Instruments*, 83, 033905. <https://doi.org/10.1063/1.3698000>
- Konopliv, A. S., Park, R. S., & Emakov, A. I. (2020). The Mercury gravity field, orientation, love number, and ephemeris from the MESSENGER radiometric tracking data. *Icarus*, 335, 113386. <https://doi.org/10.1016/j.icarus.2019.07.020>
- Kuwahara, H., Itoh, S., Nakada, R., & Irifune, T. (2019). The effects of carbon concentration and silicate composition on the metal-silicate partitioning of carbon in a shallow magma ocean. *Geophysical Research Letters*, 46(16), 9422–9429. <https://doi.org/10.1029/2019GL084254>
- Kuwayama, Y., & Hirose, K. (2004). Phase relations in the system Fe-FeSi at 21 GPa. *American Mineralogist*, 89(2–3), 273–276. <https://doi.org/10.2138/am-2004-2-303>
- Li, Y., Dasgupta, R., Tsuno, K., Monteleone, B., & Shimizu, N. (2016). Carbon and Sulfur budget of the silicate Earth explained by accretion of differentiated planetary embryos. *Nature Geoscience*, 9, 781–785. <https://doi.org/10.1038/ngeo2801>
- Litasov, K. D., Sharygin, I. S., Dorogokupets, P. I., Shatskiy, A., Gavryushkin, P. N., Sokolova, T. S., et al. (2013). Thermal equation of state and thermodynamic properties of iron carbide Fe<sub>3</sub>C to 31 GPa and 1473 K. *Journal of Geophysical Research: Solid Earth*, 118(10), 5274–5284. <https://doi.org/10.1002/2013JB010270>
- Malavergne, V., Cordier, P., Righter, K., Brunet, F., Zanda, B., Addad, A., et al. (2014). How Mercury can be the most reduced terrestrial planet and still store iron in its mantle. *Earth and Planetary Science Letters*, 394, 186–197. <https://doi.org/10.1016/j.epsl.2014.03.028>
- Manglik, A., Wicht, J., & Christensen, U. R. (2010). A dynamo model with double diffusive convection for Mercury. *Earth and Planetary Science Letters*, 289, 619–628. <https://doi.org/10.1016/j.epsl.2009.12.007>
- Margot, J.-L., Peale, S. J., Solomon, S. C., Hauck, S. A., II, Ghigo, F. D., Jurgens, R. F., et al. (2012). Mercury's moment of inertia from spin and gravity data. *Journal of Geophysical Research: Planets*, 117(E12). <https://doi.org/10.1029/2012JE004161>
- Mazarico, E., Genova, A., Goossens, S., Lemoine, F. G., Neumann, G. A., Zuber, M. T., et al. (2014). The gravity field, orientation, and ephemeris of Mercury from MESSENGER observations after three years in orbit. *Journal of Geophysical Research: Planets*, 119(12), 2417–2436. <https://doi.org/10.1002/2014JE004675>
- McCoy, T. J., Dickinson, T. L., & Lofgren, G. E. (1999). Partial melting of the Indarch (EH4) meteorite: A textural, chemical, and phase relations view of melting and melt migration. *Meteoritics and Planetary Science*, 34(5), 735–746. <https://doi.org/10.1111/j.1945-5100.1999.tb01386.x>
- McCubbin, F. M., Vander Kaaden, K. E., Peplowski, P. N., Bell, A. S., Nittler, L. R., Boyce, J. W., et al. (2017). A low O/Si ratio on the surface of Mercury: Evidence for silicon smelting? *Journal of Geophysical Research: Planets*, 122(10), 2053–2076. <https://doi.org/10.1002/2017JE005367>



- Michel, N. C., Hauck, S. A., II, Solomon, S. C., Phillips, R. J., Roberts, J. H., & Zuber, M. T. (2013). Thermal evolution of Mercury as constrained by MESSENGER observations. *Journal of Geophysical Research: Planets*, 118(5), 1033–1044. <https://doi.org/10.1002/jgre.20049>
- Morard, G., Andrault, D., Guignot, N., Siebert, J., Garbarino, G., & Antonangeli, D. (2011). Melting of Fe-Ni-Si and Fe-Ni-S alloys at megabar pressures: Implications for the core-mantle boundary temperature. *Physics and Chemistry of Minerals*, 38, 767–776. <https://doi.org/10.1007/s00269-011-0449-9>
- Morard, G., Bouchet, J., Rivoldini, A., Antonangeli, D., Roberge, M., Boulard, E., et al. (2018). Liquid properties in the Fe-FeS system under moderate pressure: Tool box to model small planetary cores. *American Mineralogist*, 103(11), 1770–1779. <http://dx.doi.org/10.2138/am-2018-6405>
- Morard, G., Siebert, J., Andrault, D., Guignot, N., Garbarino, G., Guyot, F., & Antonangeli, D. (2013). The Earth's core composition from high pressure density measurements of liquid iron alloys. *Earth and Planetary Science Letters*, 373, 169–178. <https://doi.org/10.1016/j.epsl.2013.04.040>
- Nakajima, Y., Imada, S., Hirose, K., Komabayashi, T., Ozawa, H., Tateno, S., et al. (2015). Carbon-depleted outer core revealed by sound velocity measurements of liquid iron-carbon alloy. *Nature Communications*, 6(1), 1–7. <https://doi.org/10.1038/ncomms9942>
- Namur, O., & Charlier, B. (2017). Silicate mineralogy at the surface of Mercury. *Nature Geoscience*, 10, 9–13. <https://doi.org/10.1038/ngeo2860>
- Namur, O., Charlier, B., Holtz, F., Cartier, C., & McCammon, C. (2016). Sulfur Solubility in reduced mafic silicate melts: Implications for the speciation and distribution of sulfur on Mercury. *Earth and Planetary Science Letters*, 448, 102–114. <https://doi.org/10.1016/j.epsl.2016.05.024>
- Ness, N. F. (1979). The magnetic field of Mercury. *Physics of the Earth and Planetary Interiors*, 20(2–4), 209–217. [https://doi.org/10.1016/0031-9201\(79\)90044-X](https://doi.org/10.1016/0031-9201(79)90044-X)
- Nittler, L. R., Chabot, N. L., Grove, T. L., & Peplowski, P. N. (2018). The chemical composition of Mercury. In S. C. Solomon, L. R. Nittler, & B. J. Anderson (Eds.), *Mercury: The view after MESSENGER* (Ch 2, pp. 30–51). Cambridge University Press, Cambridge.
- Nittler, L. R., Starr, R. D., Weider, S. Z., McCoy, T. J., Boynton, W. V., Ebel, D. S., et al. (2011). The major-element composition of Mercury's surface from MESSENGER X-ray spectrometry. *Science*, 333(6051), 1847–1850. <https://doi.org/10.1126/science.1211567>
- Padovan, S., Wiecek, M. A., Margot, J.-L., Tosi, N., & Solomon, S. C. (2015). Thickness of the crust of Mercury from geoid-to-topography ratios. *Geophysical Research Letters*, 42(4), 1029–1038. <https://doi.org/10.1002/2014GL062487>
- Peale, S. J. (1981). Measurements accuracies required for the determination of a Mercurian liquid core. *Icarus*, 48(1), 143–145. [https://doi.org/10.1016/0019-1035\(81\)90160-3](https://doi.org/10.1016/0019-1035(81)90160-3)
- Peale, S. J., Margot, J.-L., Hauck, S. A., II, & Solomon, S. C. (2016). Consequences of a solid inner core on Mercury's spin configuration. *Icarus*, 264, 443–455. <https://doi.org/10.1016/j.icarus.2015.09.024>
- Peiris, S. M., Campbell, A. J., & Heinz, D. L. (1994). Compression of MgS to 54 GPa. *Journal of Physics and Chemistry of Solids*, 55(5), 413–419. [https://doi.org/10.1016/0022-3697\(94\)90166-X](https://doi.org/10.1016/0022-3697(94)90166-X)
- Peplowski, P. N., Evans, L. G., Hauck, S. A., II, McCoy, T. J., Boynton, W. V., Gillis-Davis, J. J., et al. (2011). Radioactive elements on Mercury's surface from MESSENGER: Implications for the planet's formation and evolution. *Science*, 333(6051), 1850–1852. <https://doi.org/10.1126/science.1211576>
- Peplowski, P. N., Evans, L. G., Stockstill-cahill, K. R., Lawrence, D. J., Goldsten, J. O., McCoy, T. J., et al. (2014). Enhanced sodium abundance in Mercury's north polar region revealed by the MESSENGER Gamma-Ray Spectrometer. *Icarus*, 228, 86–95. <https://doi.org/10.1016/j.icarus.2013.09.007>
- Peplowski, P. N., Lawrence, D. J., Evans, L. G., Klima, R. L., Blewett, D. T., Goldsten, J. O., et al. (2015). Constraints on the abundance of carbon in near-surface materials on Mercury: Results from the MESSENGER Gamma-Ray Spectrometer. *Planetary and Space Science*, 108, 98–107. <https://doi.org/10.1016/j.pss.2015.01.008>
- Petaev, M. I., Meibom, A., Krot, A. N., Wood, J. A., & Keil, K. (2001). The condensation origin of zoned metal grains in Queen Alexandra Range 94411: Implications for the formation of the Bencubbin-like chondrites. *Meteoritics and Planetary Science*, 36(1), 93–106. <https://doi.org/10.1111/j.1945-5100.2001.tb01812.x>
- Pronin, L. A., Kazakov, N. V., & Filippov, S. I. (1964). Izvestia Vuzov. *Chemaya Metallurgiya*, 5, 12–16. (in Russian)
- Rabe, E. (1950). Derivation of fundamental astronomical constants from the observations of Eros during 1926–1945. *The Astronomical Journal*, 55, 112–125. <https://doi.org/10.1086/106364>
- Rivoldini, A., & Van Hoolst, T. (2013). The interior structure of Mercury constrained by the low-degree gravity field and the rotation of Mercury. *Earth and Planetary Science Letters*, 377–378, 62–72. <https://doi.org/10.1016/j.epsl.2013.07.021>
- Sanloup, A., Fiquet, G., Gregoryanz, E., Morard, G., & Mezouar, M. (2004). Effect of Si on liquid compressibility: Implications for sound velocity in core materials. *Geophysical Research Letters*, 31(7). <https://doi.org/10.1029/2004GL019526>
- Sanloup, C., van Westrenen, W., Dasgupta, R., Maynard-Casely, H., & Perrillat, J.-P. (2011). Compressibility change in iron-rich melt and implications for core formation models. *Earth and Planetary Science Letters*, 306(1–2), 118–122. <https://doi.org/10.1016/j.epsl.2011.03.039>
- Shimoyama, Y., Terasaki, H., Urakawa, S., Takubo, Y., Kuwabara, S., Kishimoto, S., et al. (2016). Thermoelastic properties of liquid Fe-C revealed by sound velocity and density measurements at high pressure. *Journal of Geophysical Research: Solid Earth*, 121(11), 7984–7995. <https://doi.org/10.1002/2016JB012968>
- Silber, R. E., Secco, R. A., Yong, W., & Littleton, J. A. H. (2018). Electrical resistivity of liquid Fe to 12 GPa: Implications for heat flow in cores of terrestrial bodies. *Scientific Reports*, 8, 10758. <https://doi.org/10.1038/s41598-018-28921-w>
- Smith, D. E., Zuber, M. T., Phillips, R. J., Solomon, S. C., Hauck, S. A., II, Lemoine, F. G., et al. (2012). Gravity field and internal structure of Mercury from MESSENGER. *Science*, 336(6078), 214–217. <https://doi.org/10.1126/science.1218809>
- Stark, A., Oberst, J., Preusker, F., Peale, S. J., Margot, J.-L., Phillips, R. J., et al. (2015). First MESSENGER orbital observations of Mercury's librations. *Geophysical Research Letters*, 42, 7881–7889. <https://doi.org/10.1002/2015GL065152>
- Steenstra, E. S., & van Westrenen, W. (2020). Geochemical constraints on core-mantle differentiation in Mercury and the aubrite parent body. *Icarus*, 340, 113621. <https://doi.org/10.1016/j.icarus.2020.113621>
- Stixrude, L., & Lithgow-Bertollini, C. (2011). Thermodynamics of mantle minerals – II. Phase equilibria. *Geophysical Journal International*, 184(3), 1180–1213. <https://doi.org/10.1111/j.1365-246X.2010.04890.x>
- Steenstra, E. S., Seegers, A. X., Putter, R., Berndt, J., Klemme, S., Matveev, S., et al. (2020). Metal-silicate partitioning systematics of siderophile elements at reducing conditions: A new experimental database. *Icarus*, 335, 113391. <http://dx.doi.org/10.1016/j.icarus.2019.113391>
- Takahashi, F., Shimizu, H., & Tsunakawa, H. (2019). Mercury's anomalous magnetic field caused by a symmetry-breaking self-regulating dynamo. *Nature Communications*, 10, 208. <https://doi.org/10.1038/s41467-018-08213-7>

- Tateyama, R., Ohtani, E., Terasaki, H., Nishida, K., Shibazaki, Y., Suzuki, A., & Kikegawa, T. (2011). Density measurements of liquid Fe-Si alloys at high pressure using the sink-float method. *Physics and Chemistry of Minerals*, 38(10), 801–807. <https://doi.org/10.1007/s00269-011-0452-1>
- Taylor, G. J., & Scott, E. R. D. (2003). Mercury. In H. H. Holland, & K. K. Turekian (Eds.), *Treatise on geochemistry* (Ch. 1.18, pp. 477–485). Amsterdam, Netherlands: Elsevier. <https://doi.org/10.1016/B0-08-043751-6/01071-9>
- Terasaki, H., Nishida, K., Shibazaki, Y., Sakamaki, T., Suzuki, A., Ohtani, E., & Kikegawa, T. (2010). Density measurements of Fe<sub>3</sub>C liquid using X-ray absorption image up to 10 GPa and effect of light elements on compressibility of liquid iron. *Journal of Geophysical Research: Solid Earth*, 115(B6). <https://doi.org/10.1002/2009JB006905>
- Terasaki, H., Rivoldini, A., Shimoyama, Y., Nishida, K., Urakawa, S., Maki, M., et al. (2019). Pressure and compositions effects on sound velocity and density of core-forming liquids: Implication to core compositions of terrestrial planets. *Journal of Geophysical Research: Planets*, 124(8), 2272–2293. <https://doi.org/10.1029/2019JE005936>
- Tian, Z., Zuber, M. T., & Stanley, S. (2015). Magnetic field modelling for Mercury using dynamo models with a stable layer and laterally variable heat flux. *Icarus*, 260, 263–268. <https://doi.org/10.1016/j.icarus.2015.07.019>
- Tosi, N., Grott, M., Plesa, A.-C., & Breuer, D. (2013). Thermochemical evolution of Mercury's interior. *Journal of Geophysical Research: Planets*, 118(12), 2474–2487. <https://doi.org/10.1002/jgre.20168>
- Urakawa, S., Someya, K., Terasaki, H., Katsura, T., Yokoshi, S., Funakoshi, K., et al. (2004). Phase relationships and equations of state for FeS at high pressures and temperatures and implications for the internal structure of Mars. *Physics of the Earth and Planetary Interiors*, 143–144, 469–479. <https://doi.org/10.1016/j.pepi.2003.12.015>
- Urey, H. C. (1951). The origin and development of the earth and other terrestrial planets. *Geochimica et Cosmochimica Acta*, 1(4–6), 209–277. [https://doi.org/10.1016/0016-7033\(51\)90001-4](https://doi.org/10.1016/0016-7033(51)90001-4)
- Van Hoolst, T., Rivoldini, A., Baland, R.-M., & Yseboodt, M. (2012). The effect of tides and an inner core on the forced longitudinal libration of Mercury. *Earth and Planetary Science Letters*, 333–334, 83–90. <https://doi.org/10.1016/j.epsl.2012.04.014>
- van Kan-Parker, M., Sanloup, C., Tronche, E. J., Perrilat, J.-P., Mezouar, M., Rai, N., & van Westrenen, W. (2010). Calibration of a diamond capsule cell assembly for in situ determination of liquid properties in the Paris-Edinburgh press. *High Pressure Research*, 30(2), 332–341. <https://doi.org/10.1080/08957959.2010.484283>
- Vander Kaaden, K. E., & McCubbin, F. (2015). Exotic crust formation on Mercury: Consequences of a shallow, FeO-poor mantle. *Journal of Geophysical Research: Planets*, 120(2), 195–209. <https://doi.org/10.1002/2014JE004733>
- Vander Kaaden, K. E., McCubbin, F. M., Nittler, L. R., Peplowski, P. N., Weider, S. Z., Frank, E. A., & McCoy, T. J. (2017). Geochemistry, mineralogy, and petrology of boninitic and komatiitic rocks on the Mercurian surface: Insights into the Mercurian mantle. *Icarus*, 285, 155–168. <https://doi.org/10.1016/j.icarus.2016.11.041>
- Vander Kaaden, K. E., McCubbin, F. M., Turner, A. A., & Kent Ross, D. (2020). Constraints on the abundances of carbon and silicon in Mercury's core from experiments in the Fe-Si-C system. *Journal of Geophysical Research: Planets*, 125(5), e2019JE006239. <https://doi.org/10.1029/2019JE006239>
- Vilim, R., Stanley, S., & Hauck, S. A., II (2010). Iron snow zones as a mechanism for generating Mercury's weak observed magnetic field. *Journal of Geophysical Research: Planets*, 115(E11). <https://doi.org/10.1029/2009JE003528>
- Wagle, F., & Steinle-Neumann, G. (2019). Liquid iron equation of state to the terapascal regime from Ab initio simulations. *Journal of Geophysical Research: Solid Earth*, 124(4), 3350–3364. <https://doi.org/10.1029/2018JB016994>
- Wakabayashi, D., & Funamori, N. (2015). Solving the problem of inconsistency in the reported equations of state for h-BN. *High Pressure Research*, 35(2), 123–129. <https://doi.org/10.1080/08957959.2015.1028931>
- Wardinski, I., Amit, H., Langlais, B., & Thébault, E. (2020). The internal structure of Mercury's core inferred from magnetic observations. *Earth and Space Science Open Archive*. <https://doi.org/10.1002/essoar.10503385.1>
- Watanabe, M., Adachi, M., & Fukuyama, H. (2016). Densities of Fe-Ni melts and thermodynamic correlations. *Journal of Materials Science*, 51, 3303–3310. <https://doi.org/10.1007/s10853-015-9644-2>
- Weidenschilling, S. J. (1978). Iron/silicate fractionation and the origin of Mercury. *Icarus*, 35(1), 99–111. [https://doi.org/10.1016/0019-1035\(78\)90064-7](https://doi.org/10.1016/0019-1035(78)90064-7)
- Weider, S. Z., Nittler, L. R., Starr, R. D., McCoy, T. J., Stockstill-Cahill, K. R., Byrne, P. K., et al. (2012). Chemical heterogeneity on Mercury's surface revealed by the MESSENGER X-Ray Spectrometer. *Journal of Geophysical Research: Planets*, 117(E12). <https://doi.org/10.1029/2012JE004153>
- Weisberg, M. K., Prinz, M., Clayton, R. N., Mayeda, T. K., Sugiura, N., Zashu, S., & Ebihara, M. (2001). A new metal-rich chondrite grouplet. *Meteoritics and Planetary Science*, 36(3), 401–418. <https://doi.org/10.1111/j.1945-5100.2001.tb01882.x>
- Weyrauch, M., Zipfel, J., & Weyer, S. (2019). Origin of metal from CB chondrites in an impact plume – a combined study of Fe and Ni isotope composition and trace element abundances. *Geochimica et Cosmochimica Acta*, 246, 123–137. <https://doi.org/10.1016/j.gca.2018.11.022>
- Williams, Q., Manghani, M. H., Secco, R. A., & Fu, S. (2015). Limitations on silicon in the outer core: Ultrasonic measurements at high temperature and high dK/dP values of Fe-Ni-Si liquids at high pressures. *Journal of Geophysical Research: Solid Earth*, 120(10), 6846–6855. <https://doi.org/10.1002/2015JB012270>
- Wurm, G., Trierloff, M., & Rauer, H. (2013). Photophoretic separation of metals and silicates: The formation of Mercury-like planets and metal depletion in chondrites. *The Astrophysical Journal*, 769(1), 78. <https://doi.org/10.1088/0004-637X/769/1/78>
- Yu, X., & Secco, R. A. (2008). Equation of state of liquid Fe-17 wt% Si to 12 GPa. *High Pressure Research*, 28(1), 19–28. <https://doi.org/10.1080/08957950701882138>
- Zolotov, M. Y., Sprague, A. L., Hauck, S. A., Nittler, L. R., Solomon, S. C., & Weider, S. Z. (2013). The redox state, FeO content, and origin of sulfur-rich magmas on Mercury. *Journal of Geophysical Research: Planets*, 118(1), 138–146. <https://doi.org/10.1029/2012JE004274>

## References from the Supporting Information

- Blairs, S. (2007). Review of data for velocity of sound in pure liquid metals and metalloids. *International Materials Reviews*, 52(6), 321–344. <https://doi.org/10.1179/174328007X212490>
- Griffing, V., Cargyle, M. A., Corvese, L., Eby, D. (1954). Temperature coefficients of viscosity of some halogen substituted organic compounds. *The Journal of Physical Chemistry*, 58(11), 1054–1056. <https://doi.org/10.1021/j150521a032>
- Neuville, D. R. (2006). Viscosity, structure, and mixing in (Ca, Na) silicate melts. *Chemical Geology*, 229(1–3), 28–41. <https://doi.org/10.1061/j.chemgeo.2006.01.008>

- Verma, A. K., Margot, J.-L. (2016). Mercury's gravity, tides, and spin from MESSENGER radio science data. *Journal of Geophysical Research: Planets*, 121, 1627–1640. <https://doi.org/10.1002/2016JE005037>
- Weber, R. C., Lin, P.-Y., Garnero, E. J., Williams, Q., & Lognonné, P. Z. (2011). *Seismic detection of the lunar core*. *Science*, 331(6015), 309–312. <https://doi.org/10.1126/science.1199375>
- Yamashita, T., Tanaka, Y., Nagoshi, M., & Ishida, K. (2016). Novel technique to suppress hydrocarbon contamination for high accuracy determination of carbon content in steel by FE-EPMA. *Scientific Reports*, 6, 29825. <https://doi.org/10.1038/srep29825>